CEDAR-GPP: spatiotemporally upscaled estimates of gross primary productivity incorporating CO_2 fertilization

Yanghui Kang[1,2], Maoya Bassiouni[1,2], Max Gaber[1,3], Xinchen Lu[1,2], Trevor F. Keenan[1,2]

[1] Department of Environmental Science, Policy, and Management, University of California, Berkeley, Berkely, CA 94720, USA

[2] Climate and Ecosystem Sciences Division, Lawrence Berkeley National Laboratory, Berkeley, CA 94720, USA

[3] Department of Geosciences and Natural Resource Management, University of Copenhagen, Copenhagen, 1350, Denmark.

Correspondence: Yanghui Kang (yanghuikang@berkeley.edu)
Trevor Keenan (trevorkeenan@berkeley.edu)

Abstract: Gross primary productivity (GPP) is the largest carbon flux in the Earth system, playing a crucial role in removing atmospheric carbon dioxide and providing carbohydrates needed for ecosystem metabolism. Despite the importance of GPP, however, existing estimates present significant uncertainties and discrepancies. A key issue is the underrepresentation of the CO_2 fertilization effect, a major factor contributing to the increased terrestrial carbon sink over recent decades. This omission could potentially bias our understanding of ecosystem responses to climate change.

Here, we introduce CEDAR-GPP, the first global machine-learning-upscaled GPP product that incorporates the direct CO_2 fertilization effect on photosynthesis. Our product is comprised of monthly GPP estimates and their uncertainty at 0.05° resolution from 1982 to 2020, generated using a comprehensive set of eddy covariance measurements, multi-source satellite observations, climate variables, and machine learning models. Importantly, we used both theoretical and data-driven approaches to incorporate the direct CO_2 effects. Our machine learning models effectively predicted monthly GPP (R^2 ~ 0.74), the mean seasonal cycles (R^2 ~ 0.79), and spatial variabilities (R^2 ~ 0.67) based on cross-validation at flux sites. Incorporation of the direct CO_2 effects substantially enhanced the predicted long-term trend in GPP across global flux towers by up to 51%, aligning much closer

to a strong positive trend from eddy covariance data. While the global patterns of annual mean GPP, seasonality, and interannual variability generally aligned with existing satellite-based products, CEDAR-GPP demonstrated higher long-term trends globally after incorporating CO_2 fertilization, particularly in the tropics, reflecting a strong temperature control on direct CO_2 effects. CEDAR-GPP offers a comprehensive representation of GPP temporal and spatial dynamics, providing valuable insights into ecosystem-climate interactions. The CEDAR-GPP product is available at https://zenodo.org/doi/10.5281/zenodo.8212706 (Kang et al., 2024).

1. Introduction

Terrestrial ecosystem photosynthesis, known as Gross Primary Productivity (GPP), is the primary source of food and energy for the Earth system and human society (Keenan and Williams, 2018). Through photosynthesis, terrestrial ecosystems also mitigate climate change, by removing thirty percent of anthropogenic carbon emissions from the atmosphere each year (Friedlingstein et al., 2023). However, due to the lack of direct measurements at the global scale, our understanding of photosynthesis and its spatiotemporal dynamics is limited, leading to considerable disagreements among various GPP estimates (Anav et al., 2015; O'Sullivan et al., 2020; Smith et al., 2016; Yang et al., 2022). Addressing these uncertainties is crucial for improving the predictability of ecosystem dynamics under climate change (Friedlingstein et al., 2014).

Over the past three decades, global networks of eddy covariance flux towers collected *in situ* carbon flux measurements that allow for accurate estimates of GPP, providing valuable insights into photosynthesis dynamics under various environmental conditions (Baldocchi, 2020; Beer et al., 2010). To quantify and understand GPP at scales and locations beyond the ~ $1km^2$ flux tower footprints, machine learning has been employed with gridded satellite and climate datasets to upscale site-based measurements and produce wall-to-wall GPP maps (Dannenberg et al., 2023; Joiner and Yoshida, 2020; Jung et al., 2011; Tramontana et al., 2016; Xiao et al., 2008; Yang et al., 2007; Zeng et al., 2020). This "upscaling" approach provides data-driven and observation-based quantifications without prescribed functional relations between GPP and its climatic or environmental drivers. It offers unique empirical constraints of ecosystem carbon dynamics, complementing those derived from process-based and semi-process-based approaches such as terrestrial biosphere models or the Light Use Efficiency (LUE) models (Beer et al., 2010; Gampe et al., 2021; Jung et al., 2017; Schwalm et al., 2017). In recent years, the growth of global and regional flux networks, coupled with increasing efforts in data standardization, has offered new opportunities for the advancement of upscaling frameworks, enabling comprehensive quantifications of terrestrial photosynthesis (Joiner and Yoshida, 2020; Pastorello et al., 2020).

Effective machine learning upscaling depends on a complete set of input predictors that fully explain GPP dynamics. Upscaled datasets have primarily relied on satellite-observed greenness indicators, such as vegetation indices, Leaf Area Index (LAI), the fraction of absorbed photosynthetically active radiation (fAPAR), which effectively capture canopy-level GPP dynamics related to leaf area changes (Joiner and Yoshida, 2020; Ryu et al., 2019; Tramontana et al., 2016).

However, important aspects of leaf-level physiology, such as those controlled by climate factors, are often omitted in major upscaled datasets, preventing accurate characterization of GPP responses to climate change (Bloomfield et al., 2023; Stocker et al., 2019). In particular, none of the previous upscaled datasets have considered the direct effect of atmospheric CO_2 on leaf-level photosynthesis, which is a key factor contributing to at least half of the enhanced land carbon sink observed over the past decades (Keenan et al., 2016, 2023; Ruehr et al., 2023; Walker et al., 2021). This omission can lead to incorrect inferences regarding long-term trends in various components of the terrestrial carbon cycle (De Kauwe et al., 2016).

Multiple independent lines of evidence from the atmospheric inversion (Wenzel et al., 2016), atmospheric $^{13}C/^{12}C$ measurements (Keeling et al., 2017), ice core records of carbonyl sulfide (Campbell et al., 2017), glucose isotopomers (Ehlers et al., 2015), as well as free-air CO_2 enrichment experiments (FACE) (Walker et al., 2021), suggest a widespread positive effect of elevated atmospheric CO_2 on GPP from site to global scales. Increasing atmospheric CO_2 *directly* stimulates the biochemical rate or the light use efficiency (LUE) of leaf-level photosynthesis, known as the direct CO_2 fertilization effect (CFE). Enhanced photosynthesis could lead to greater net carbon assimilation, contributing to an increase in total leaf area. This expansion, contributing to a higher light interception, further enhances canopy-level photosynthesis (i.e. GPP), which is referred to as the indirect CFE. The direct CFE has been found to dominate GPP responses to CO_2 compared to the indirect effect, from both theoretical and observational analyses (Chen et al., 2022; Haverd et al., 2020).

Satellite-based estimates have shown an increasing global GPP trend in the past few decades largely attributable to CO_2-induced increases in LAI (Chen et al., 2019; De Kauwe et al., 2016; Piao et al., 2020; Zhu et al., 2016). However, previous upscaled GPP datasets, as well as most LUE models such as the MODIS GPP product, have failed to consider the direct CO_2 effects on leaf-level biochemical processes (Jung et al., 2020; Zheng et al., 2020). Consequently, these products likely underestimated the long-term trend of global GPP, leading to large discrepancies when compared to process-based models, which typically consider both direct and indirect CO_2 effects (Anav et al., 2015; De Kauwe et al., 2016; Keenan et al., 2023; O'Sullivan et al., 2020). Notably, recent improvements in LUE models have included the CO_2 response and show improved long-term changes in GPP globally (Zheng et al., 2020), yet, this important mechanism is still missing in GPP products upscaled from *in situ* eddy covariance flux measurements based on machine learning models.

To improve the quantification of GPP spatial and temporal dynamics and provide a robust representation of long-term dynamics in global photosynthesis, we developed the CEDAR-GPP[1] data product. CEDAR-GPP was upscaled from global eddy covariance carbon flux measurements using machine learning along with a broad range of multi-source satellite observations and climate variables. In addition to incorporating direct CO_2 fertilization effects on photosynthesis, we also account for indirect effects via greenness indicators and include novel satellite datasets such as solar-induced fluorescence (SIF), Land Surface Temperature (LST) and soil moisture to explain variability under environmental stresses. We provide monthly GPP estimations and associated uncertainties at 0.05° resolution derived from ten model setups. These setups differ by the temporal range depending on satellite data availability, the method for incorporating the direct CO_2 fertilization effects, and the partitioning approach used to derive GPP from eddy covariance measurements. Short-term model setups were primarily based on data derived from MODIS satellites generating GPP estimates from 2001 to 2020, while long-term estimates spanned 1982 to 2020 using combined Advanced Very High Resolution Radiometer (AVHRR) and MODIS data. We used two approaches to incorporate the direct CO_2 fertilization effects, including direct prescription with eco-evolutionary theory and machine learning inference from the eddy-covariance data. Additionally, we provided a baseline configuration that did not incorporate the direct CO_2 effects. Uncertainties in GPP estimation were quantified using bootstrapped model ensembles. We evaluated the machine learning models' skills in predicting monthly GPP, seasonality, interannual variability, and trend against eddy covariance measurements, and compared the CEDAR-GPP spatial and temporal variability to existing satellite-based GPP estimates.

2. Data and Methods

2.1 Eddy covariance data

We obtained monthly eddy covariance GPP measurements from 2001 to 2020 from the FLUXNET2015 (Pastorello et al., 2020), AmeriFlux FLUXNET (https://ameriflux.lbl.gov/data/flux-data-products/), and ICOS Warm Winter 2020 (Warm Winter 2020 Team, 2022) datasets. All data were processed with the ONEFLUX pipeline (Pastorello et al., 2020). Following previous upscaling efforts (Tramontana et al., 2016), we selected monthly GPP

[1] CEDAR stands for upsCaling Ecosystem Dynamics with ARtificial inteligence

data with at least 80% of high-quality hourly or half-hourly data for temporal aggregation. We further excluded large negative GPP values, setting a cutoff of -1 $gCm^{-2}d^{-1}$. We utilized GPP estimates from both the night-time (GPP_REF_NT_VUT) and day-time (GPP_REF_DT_VUT) partitioning approaches. We classified flux tower sites according to the C3 and C4 plant categories reported in metadata and related publications when available and used a C4 plant percentage map (Still et al., 2003) otherwise. Our analysis encompassed 233 sites, predominately located in North America, Western Europe, and Australia (Figure 1, Table S1). Despite their uneven geographical distribution, these sites effectively cover a diverse range of climatic conditions and are representative of global biomes (Figure 1c, 1d). In total, our dataset included over 18000 site-months. Note that we did not include eddy covariance data before 2001, since it was limited to only a few sites with only four sites containing data before 1996. This scarcity might introduce biases in the machine learning models, particularly in the relationship between GPP and CO_2, leading to unreliable extrapolations across space and time in the long-term predictions.

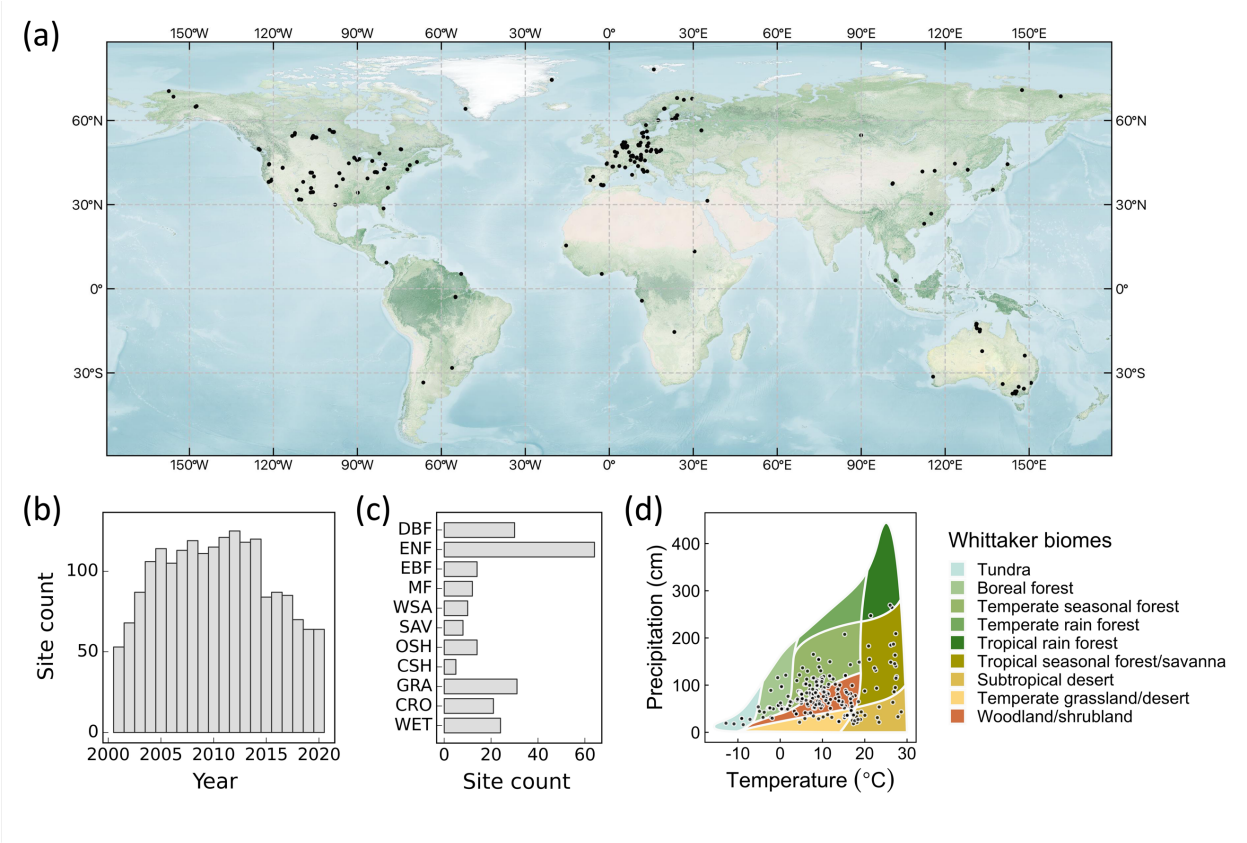

Figure 1. (a) Spatial distribution of eddy covariance sites used to generate the CEDAR-GPP product. (b) Annual site counts. (c) Site counts by biomes. ENF: evergreen needleleaf forests, EBF: evergreen broadleaf forests, DBF: deciduous broadleaf forests, MF: mixed forests, WSA: woody savannas, SAV: savannas, OSH: open shrublands,

CSH: closed shrublands, GRA: grasslands, CRO: croplands, WET: wetlands. (d) Sites distributions in the annual temperature and precipitation space. Whittaker biome classification is shown as a reference of natural vegetation based on long-term climatic conditions. It does not directly indicate the actual biome associated with each site. The base map in (a) was obtained from the NASA Earth Observatory map by Joshua Stevens using data from NASA's MODIS Land Cover, the Shuttle Radar Topography Mission (SRTM), the General Bathymetric Chart of the Oceans (GEBCO), and Natural Earth boundaries. Whittaker biomes were plotted using the "plotbiomes" R package (Ştefan and Levin, 2018).

2.2 Global input datasets

We compiled an extensive set of covariates from gridded climate reanalysis data, multi-source satellite datasets including optical, thermal, and microwave observations, as well as categorical information on land cover, climate zone, and C3/C4 classification. The datasets that we compiled offer comprehensive information about GPP dynamics and its responses to climatic variabilities and stresses. Table 1 lists the datasets and associated variables used to generate CEDAR-GPP.

Table 1. Datasets and input variables used to generate the CEDAR GPP product. For a list of selected variables used in different model setups, please refer to Table S1.

Category	Dataset	Temporal coverage	Spatial resolution	Temporal resolution	Variables	Reference
Climate	ERA5-Land Monthly Averaged data	1950 – present	0.1°	Monthly	Air temperature; vapor pressure deficit, Precipitation, Air and skin temperature, surface downwelling solar radiation, Potential evaporation	(Sabater, 2019)
	ESRA Global Monitoring Laboratory Atmospheric Carbon Dioxide	1976 – present	-	Monthly	Atmospheric CO_2 concentration averaged from Mauna Loa, Hawaii, US and South Pole, Antarctica	(Thoning et al., 2021)
Satellite-based datasets	MODIS Nadir BRDF-adjusted reflectance (MCD43C4v006)	2000 – present	0.05°	Daily	Surface reflectance b1 – b7, Vegetation indices (NIRv, NDVI, kNDVI, EVI, CIgreen, NDWI), percent snow	(Schaaf and Wang, 2015)
	MODIS Terra and Aqua	2000 – present	500m	4-day, 8-day	LAI, fPAR	(Myneni et al., 2015a, b)

	LAI/fPAR (MCD15A3H, MOD15A2H, v006)					
	MODIS Terra and Aqua LST (MYD11A1, MOD11A1, v006)	2000 – present	1 km	Daily	Daytime LST Nighttime LST	(Wan et al., 2015b, a)
	BESS_Rad	2000 – 2020	0.05º	Daily	PAR, diffuse PAR, downwelling solar radiation	(Ryu et al., 2018)
	Continuous-SIF (from OCO-2 and MODIS)	2000 – 2020	0.05º	4-day	all-sky daily average SIF	(Zhang, 2021)
	ESA CCI Soil Moisture Combined Passive and Active (v06.1)	1979 – 2021	0.25º	Daily	Surface soil moisture	(Gruber et al., 2019)
	GIMMS LAI4g	1982 – 2021	0.0833º	Half-month	LAI	(Cao et al., 2023)
	GIMMS NDVI4g	1982 – 2021	0.0833 º	Half-month	NDVI	(Li et al., 2023)
Static categorical datasets	MODIS Land Cover (MCD12Q1v006)	Average status used between 2001 and 2020	500m	-	Plant function types	(Friedl and Sulla-Menashe, 2019)
	Koppen-Geiger Climate Classification	present	1 km	-	Koppen-Geiger climate classes	(Beck et al., 2018)
	C4 percentage map	present	1º	-	Percentage of C4 plants	(Still et al., 2003, 2009)

2.2.1 Climate variables

We obtained air temperature, vapor pressure deficit, precipitation, potential evapotranspiration, and skin temperature from the EAR5-Land reanalysis dataset (Sabater, 2019) (Table 1; Table S1). We applied a three-month lag to precipitation, to reflect the memory of soil moisture and represent the root zone water availability. Averaged monthly atmospheric CO_2 concentrations were calculated as an average of records from the Mauna Loa Observatory and South Pole Observation stations, retrieved from NOAA's Earth System Research Laboratory (Thoning et al., 2021).

2.2.2 Satellite datasets

We assembled a broad collection of satellite-based observations of vegetation greenness and structure, LST, solar radiation, solar-induced fluorescence (SIF), and soil moisture (Table 1, Table S1).

We used three MODIS version 6 products: surface reflectance, LAI/fAPAR, and LST. Surface reflectance from optical to infrared bands (band 1 to 7) was sourced from the MODIS Nadir BRDF-adjusted reflectance (NBAR) daily dataset (MCD43C4) (Schaaf and Wang, 2015). From these data, we derived vegetation indices, including NIRv (Badgley et al., 2019), kNDVI (Camps-Valls et al., 2021), NDVI, Enhanced Vegetation Index (EVI), Normalized Difference Water Index (NDWI) (Gao, 1996), and the green chlorophyll index (CIgreen) (Gitelson, 2003). We also used snow percentages from the NBAR dataset. We used the 4-day LAI and fPAR composite derived from Terra and Aqua satellites (MCD15A3H) (Myneni et al., 2015a; Yan et al., 2016a, b) from July 2002 onwards and the MODIS 8-day LAI and fPAR dataset from Terra only (MOD15A2H) prior to July 2002 (Myneni et al., 2015b). We used day-time and night-time LST from the Aqua satellite (MYD11A1) (Wan et al., 2015b), with the Terra-based LST product (MOD11A1) used after July 2002 (Wan et al., 2015a). Terra LST was bias-corrected with the differences in the mean seasonal cycles between Aqua and Terra following Walther et al. (2022).

We used the PKU GIMMS NDVI4g dataset (Li et al., 2023) and PKU GIMMS LAI4g (Cao et al., 2023) datasets available from 1982 to 2020. PKU GIMMS NDVI4g is a harmonized time series that includes AVHRR-based NDVI from 1982 to 2003 (with biases and corrections mitigated through inter-calibration with Landsat surface reflectance images) and MODIS NDVI from 2004 onward. PKU GIMMS LAI4g consisted of consolidated AVHRR-based LAI from 1982 to 2003 (generated using machine learning models trained with Landsat-based LAI data and NDVI4g) and reprocessed MODIS LAI (Yuan et al., 2011) from 2004 onwards.

We utilized photosynthetically active radiation (PAR), diffusive PAR, and shortwave downwelling radiation from the BESS_Rad dataset (Ryu et al., 2018). We obtained the continuous-SIF (CSIF) dataset (Zhang, 2021; Zhang et al., 2018) produced by a machine learning algorithm trained using OCO-2 SIF observations and MODIS surface reflectance. We used surface soil moisture from the ESA CCI soil moisture combined passive and active product (version 6.1) (Dorigo et al., 2017; Gruber et al., 2019).

2.2.3 Other categorical datasets

We used plant functional type (PFT) information derived from the MODIS Land Cover product (MCD12Q1) (Friedl and Sulla-Menashe, 2019). We followed the International Geosphere-Biosphere Program classification scheme but merged several similar categories to maximize the amount of eddy covariance sites/observations available for each category. Closed shrublands and open shrublands are combined into a shrubland category. Woody savannas and savannas are combined into savannas. We generated a static PFT map by taking the mode of the MODIS land cover time series between 2001 – 2020 at each pixel to mitigate uncertainties from misclassification in the MODIS dataset. Nevertheless, changes in vegetation structure induced by land use and land cover change are reflected in the dynamics surface reflectance and LAI/fAPAR datasets we used. We used the Koppen-Geiger main climate groups (tropical, arid, temperate, cold, and polar) (Beck et al., 2018). We also utilized a C4 plant percentage map to account for different photosynthetic pathways when incorporating CO_2 fertilization (Still et al., 2003, 2009). The C4 percentage dataset was constant over time.

2.2.4 Data preprocessing

We implemented a three-step preprocessing strategy for the satellite datasets: 1) quality control, 2) gap-filling, and 3) spatial and temporal aggregation. Firstly, we selected high-quality data based on the quality control flags of the satellite products when available. For the MODIS NBAR dataset (MCD43C3), we used data with 75% or more high-resolution NBAR pixels retrieved with full inversions for each band. For MODIS LST, we selected the best quality data from the quality control bitmask as well as data where retrieved values had an average emissivity error of no more than 0.02. For MODIS LAI/fAPAR, we used retrievals from the main algorithm with or without saturation. We used all available data in ESA-CCI soil moisture due to the presence of substantial data gaps. In the gap-filling step, missing values in satellite datasets were temporally filled at the native temporal resolution, following a two-step protocol adapted from Walther et al (2021). Short temporal gaps were first filled with medians from a moving window, and the remaining gaps were filled with the mean seasonal cycle. For datasets with a high temporal resolution, including MODIS NBAR (daily), LAI/fPAR (4-day), BESS (4-day), CSIF (4-day), ESA-CCI (daily), temporal gaps no longer than 5 days (8 days for 4-day resolution products) were filled with medians of 15-day moving windows in the first step. An exception is MODIS LST (daily), for which we used a shorter moving window of 9 days due to rapid changes in surface temperature. GIMMS LAI4g and NDVI4g data

were only filled with mean seasonal cycle due to their low temporal resolution (half-month). This is because vegetation structure could experience significant changes at half-month intervals, and gap-filling using temporal medians within moving windows could introduce considerable uncertainties and potentially over-smooth the time series. In the last processing step, all the datasets were aggregated to a monthly time step and 0.05-degree spatial resolution.

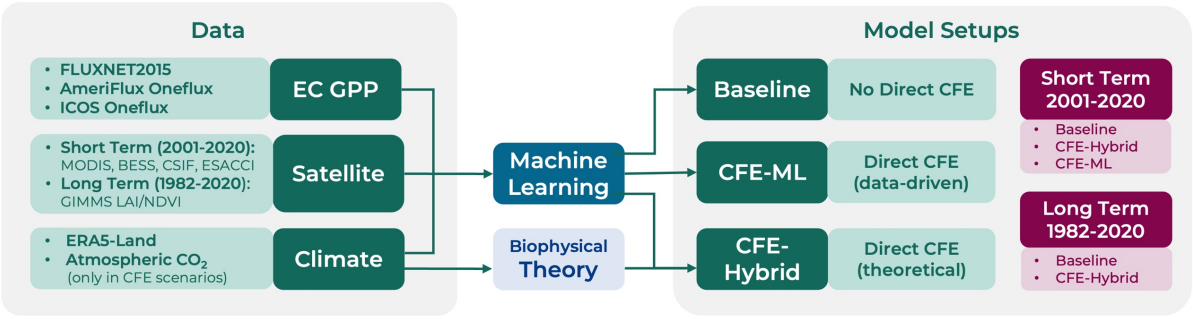

Figure 2. Schematic overview of the CEDAR-GPP model setups.

2.3 Machine learning upscaling

2.3.1 CEDAR-GPP model setups

We trained machine learning models with eddy covariance GPP measurements as targets and climate/satellite variables as input features. We created ten model setups to produce different global monthly GPP estimates (Figure 2; Table 2). The model setups were characterized by the temporal range depending on input data availability, the configuration of CO_2 fertilization effects, and the partitioning approach used to derive the GPP from eddy covariance measurements.

The short-term (ST) model configuration produced GPP from 2001 to 2020, and the long-term (LT) configuration spanned 1982 to 2020. Each temporal configuration uses a different set of input variables depending on their availability. Inputs for the short-term configuration included MODIS, CSIF, BESS PAR, ESA-CCI soil moisture, ERA5-Land, as well as PFT and Koppen Climate zone as categorical variables with one-hot encoding. The long-term used GIMMS NDVI4g and LAI4g data, ERA5-land, PFT and Koppen climate. ESA CCI soil moisture datasets were excluded from the long-term model setups due to concerns about the product quality in the early years when the number and quality of microwave satellite data were limited (Dorigo et al., 2015). A detailed list of input features for each setup is provided in Table S1.

Regarding the direct CO_2 fertilization effects (CFE), we established a "Baseline" configuration that did not incorporate these effects, a "CFE-Hybrid" configuration that incorporated the effects

via eco-evolutionary theory, and a "CFE-ML" configuration that inferred the direct effects from eddy covariance data using machine learning. Detailed information about these approaches is provided in Sec. 2.3.2. Furthermore, separate models were trained for GPP target variables from the night-time (NT) and daytime (DT) partitioning approaches.

Table 2 lists the characteristics of ten model setups. Due to the limited availability of eddy covariance observations before 2001, we did not apply the CFE-ML approach to the long-term setups. The CFE-ML model, when trained on data from 2001 to 2020 with atmospheric CO_2 ranging from 370 to 412 ppm, would not accurately predict GPP response to CO_2 for the period 1982 – 2000 when the CO2 levels were markedly lower (340 – 369 ppm). This is because machine learning models, especially tree-based models, could not extrapolate beyond the range of the training data.

Table 2. Specifications of the CEDAR-GPP model setups.

Model Setup Name	Temporal range	Direct CO_2 Fertilization Effects		GPP Partitioning Method
		Configuration	Method	
ST_Baseline_NT	Short-term (ST) 2001 – 2020	Baseline	Not incorporated	Night-time (NT)
ST_Baseline_DT				Day-time (DT)
ST_CFE-Hybrid_NT		CFE-Hybrid	Theoretical	NT
ST_CFE-Hybrid_DT				DT
ST_CFE-ML_NT		CFE-ML	Data-driven	NT
ST_CFE-ML_DT				DT
LT_Baseline_NT	Long-term (LT) 1982 – 2020	Baseline	Not incorporated	NT
LT_Baseline_DT				DT
LT_CFE-Hybrid_NT		CFE-Hybrid	Theoretical	NT
LT_CFE-Hybrid_DT				DT

2.3.2 CO_2 fertilization effect

We established three configurations regarding the direct CO_2 fertilization effects on photosynthesis. In the baseline configuration, we trained machine learning models with eddy covariance GPP measurements, input climate and satellite features, but excluding CO_2 concentration. As such, the models only include indirect CO_2 effects from the satellite-based proxies of vegetation greenness or structure representing changes in canopy light interception, and they do not consider the direct effect of CO_2 on leaf-level photosynthetic rates (or light use efficiency, LUE). Our baseline model is therefore directly comparable to other satellite-derived GPP products that only account for indirect CO2 effects (Joiner and Yoshida, 2020; Jung et al., 2020).

In the CFE-ML configuration, we added monthly CO_2 concentration into the feature set in addition to those incorporated in the baseline models. Models inferred the functional relationship between GPP and CO_2 from the eddy covariance data. They thus encompass both CO_2 fertilization pathways – direct effects on LUE and indirect effects from the satellite-based proxies of vegetation greenness and structure.

In the CFE-Hybrid configuration, we applied biophysical theory to estimate the response of LUE to elevated CO_2, i.e. the direct CFE (Appendix A). First, we estimated a reference GPP, where LUE was not affected by any increase in atmospheric CO_2, by applying the CFE-ML model with a constant atmospheric CO_2 concentration equal to the 2001 level while keeping all other variables temporally dynamic. Then, the impacts of CO_2 on LUE were prescribed onto the reference GPP estimates using a theoretical CO_2 sensitivity function of LUE according to the optimal coordination theory (Appendix A). The theoretical CO_2 sensitivity function represents a CO_2 sensitivity that is equivalent to that of the electron-transport-limited (light-limited) photosynthetic rate. When light is limited, elevated CO_2 suppresses photorespiration leading to increased photosynthesis at a lower rate than when photosynthesis is limited by CO_2 (Lloyd and Farquhar, 1996; Smith and Keenan, 2020). Thus, the CFE-Hybrid scenario provides a conservative estimation of the direct CO_2 effects on LUE. Note that the theoretical sensitivity function describes the fractional change in LUE due to direct CO_2 effects relative to a reference period (i.e. 2001). Therefore, we used the CFE-ML model to establish this reference GPP by fixing the CO_2 effects to the 2001 level, rather than simply using the GPP from the Baseline model in which the direct CO_2 effects were not represented.

For both CFE-ML and CFE-Hybrid scenarios, we made another conservative assumption that C4 plants do not benefit from elevated CO_2, despite potential increases in photosynthesis during water-limited conditions due to enhanced water use efficiency (Walker et al., 2021). Data from flux tower sites dominated by C4 plants were removed from our training set, so the machine learning models inferred CO_2 fertilization only from flux tower sites dominated by C3 plants. When applying models globally, we assumed the reference GPP values (with constant atmospheric CO_2 concentration equal to the 2001 level) to represent C4 plants, and GPP estimates from CFE-ML or CFE-Hybrid models were applied in proportion to the percentage of C3 plants in a grid cell.

2.3.3 Machine learning model training and validation

We employed the state-of-the-art XGBoost machine learning model, known for its high accuracy in regression problems across various domains, including environmental and ecological

predictions (Berdugo et al., 2022; Chen and Guestrin, 2016; Kang et al., 2020). XGBoost is a scalable and parallelized implementation of the gradient boosting technique that iteratively trains an ensemble of decision trees, with each iteration targeting to minimize the residuals from the last iteration. A notable merit of XGBoost is its ability to make prediction in the presence of missing values, a common issue in remote sensing datasets. Without relying on prior assumptions about the functional forms or statistical distributions, the model is also robust to multi-collinearity between the predictors in our dataset, particularly for the variables derived from MODIS data.

We used five-fold cross-validation for model evaluation. Training data was randomly split into five groups (folds), with each fold held out for testing while the rest four folds were used for model training. We imposed two restrictions on fold splitting: each flux site was entirely assigned to a fold to test model performance over unseen locations; the random sampling was stratified based on PFT to ensure coverage of the full range of PFTs in both training and testing. We also used a nested-cross-validation strategy, during which we performed a randomized search of hyperparameters using three-fold cross-validation within the training set. The nested-cross-validation was aimed to reduce the risk of overfitting and improve the robustness of the evaluation.

We assessed the models' ability to capture the temporal and spatial characteristics of GPP, including monthly GPP, mean seasonal cycles, monthly anomalies, and cross-site variability. Model performance was assessed separately for each model setup (Table 2) and summarized by PFT and Koppen climate zone. Mean seasonal cycles were calculated as the mean monthly GPP over the site observation period, and monthly anomalies were the residuals of monthly GPP after subtracting mean seasonal cycles. Monthly GPP averaged over years for each site was used to assess cross-site variability. Goodness-of-fit metrics include RMSE, bias, and coefficient of determination (R^2).

To evaluate the models' ability to capture long-term GPP trends, we aggregated the monthly GPP to annual values for sites with at least five years of observations following Chen et al. (2022). GPP anomalies were computed by subtracting the multi-year mean GPP from the annual GPP for each site. Anomalies were aggregated across sites to achieve a single multi-site GPP anomaly per year. We excluded a site-year if less than 11 months of data was available and used linear interpolation to fill the remaining temporal gaps. We used the Sen slope and Mann-Kendall test to examine the GPP trends from 2002 to 2019, excluding 2001 and 2020, due to the limited number of available sites with more than five years of data. We further assessed the aggregated annual trend by grouping the sites based on plant functional types and the koppen climate zones. Categories with

less than six long-term sites available were excluded from the analysis, which includes EBF and Tropics.

2.3.4 Product generation and uncertainty quantification

In the CEDAR-GPP product, we generated GPP estimates from each of the ten model setups, by applying the model to global gridded datasets within the corresponding temporal range (Table 2). GPP estimates were named after the corresponding model setups. We used bootstrapping to quantify estimate uncertainties. For each model setup, we generated 30 bootstrapped sample sets of eddy covariance data, which were then used to train an ensemble of 30 XGBoost models. The bootstrapping was performed at the site level, and each bootstrapped sample set contained around 140 to 150 unique sites, 17000 to 19000 site months covering all PFTs. The relative PFT composition in the bootstrapped sample sites was consistent with the full dataset. The 30 models trained with bootstrapped samples generated an ensemble of 30 GPP values. We provided the ensemble GPP mean and used standard deviation to indicate uncertainties, for each of the ten model setups.

2.4 Product inter-comparison

We compared the global spatial and temporal patterns of CEDAR-GPP with other major satellite-based GPP products, including three machine learning upscaled and two LUE-based datasets. We obtained two FLUXCOM products (Jung et al., 2020), the latest version of FLUXCOM-RS (FLUXCOM-RSv006) available from 2001 to 2020 based on remote sensing (MODIS collection 6) datasets only, as well as the FLUXCOM-RS+METEO ensemble available between 1979 to 2018 and based on the climatology of remote sensing observations and ERA5 forcings (hereafter FLUXCOM-ERA5). We used FluxSat (Joiner and Yoshida, 2020), available from 2001 to 2019, which is an upscaled dataset based on MODIS NBAR surface reflectance and PAR from Modern-Era Retrospective analysis for Research and Applications 2 (MERRA-2). Importantly, FluxSat does not incorporate climate forcings. We used the MODIS GPP product (MOD17) available since 2001, which was generated based on MODIS fAPAR and LUE as a function of air temperature and vapor pressure deficit but not atmospheric CO_2 concentration (Running et al., 2015). We also used the rEC-LUE products, available from 1982 to 2018 and based on a revised LUE model that incorporated the effect of atmospheric CO_2 concentration and the fraction of diffuse PAR on LUE (Zheng et al., 2020). All datasets were resampled to 0.1 ° spatial resolution, and

a common mask for the vegetated land area was applied. We evaluated global mean annual GPP, mean seasonal cycle, interannual variability, and trend among different datasets, comparing them over a common time period determined by their data availability. Global total GPP was computed by scaling the global average GPP flux with the global land area (122.4 million km2) following Jung et al. (2020). Mean seasonal cycle was defined as above (Sec. 2.3.3). We used the standard deviation of annual GPP to indicate the magnitude of interannual variability, the Sen slope to indicate the GPP annual trend, and the Mann-Kendall test for the statistical significance of trends.

3. Results

3.1 Evaluation of model performance

3.1.1 Overall performance

The short-term and long-term models explained approximately 74% and 68%, respectively, of the variation in monthly GPP across global eddy covariance sites (Figure 3a). The long-term models consistently yielded lower performance than the short-term models, likely due to differences in the satellite remote sensing datasets used, as the short-term models benefited from richer information from surface reflectance of individual bands, LST, CSIF, as well as soil moisture, while the long-term model only exploited NDVI and LAI. The models with different CFE configurations and target GPP variables (i.e. partitioning approaches) had similar performance in predicting monthly GPP (Figure 3b, Table S2). All models exhibited minimal bias of less than 0.15.

Model performance in terms of the different temporal and spatial characteristics of monthly GPP was variable (Figure 3c-h). The models were most successful at predicting mean seasonal cycles, with the short-term and long-term models explaining around 79% and 73% of the variability, respectively (Figure 3c-d). The short-term and long-term models captured 67% and 56% , respectively, of the spatial variabilities in multi-year mean GPP across global sites (i.e., cross-site variability) (Figure 3g-h). However, all models underestimated monthly anomalies across the sites, with R^2 values below 0.12 (Figure 3e-f). The CFE-ML and CFE-Hybrid models showed slightly higher accuracy than the Baseline model across all temporal and spatial characteristics in NT setups. Patterns from the DT setups do not significantly differ from those of the NT setups (Figure S1).

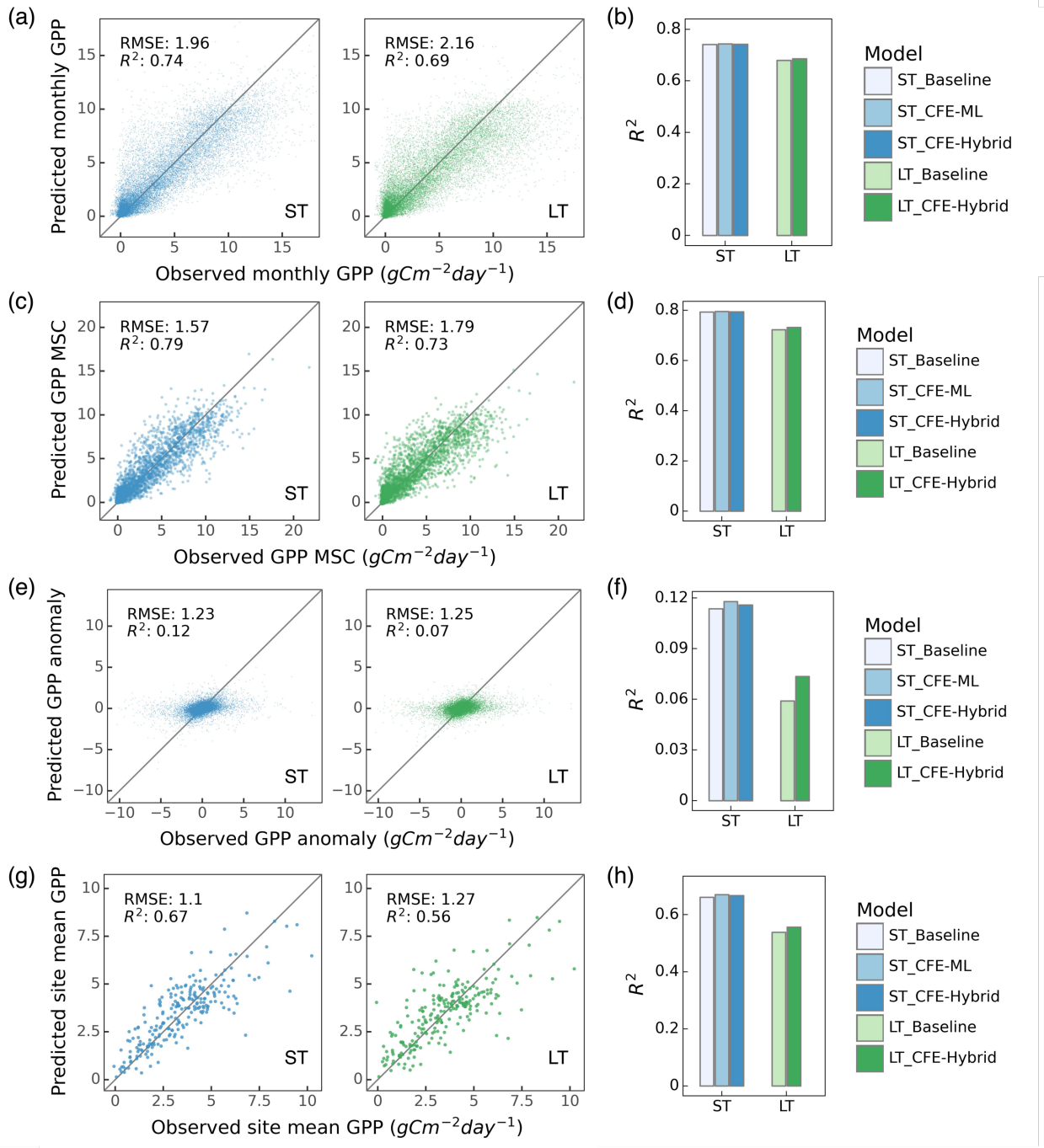

Figure 3. Machine learning model performance in predicting monthly GPP and its spatial and temporal variability. Only NT models are shown and DT results is provided in Supplementary Figure S1. Scatter plots illustrated relationships between model predictions and observations for monthly GPP (a), mean seasonal cycles (MSC) (c), monthly anomaly (e), and cross-site variability (g) for ST_CFE-Hybrid_NT (left, blue) and LT_CFE-Hybrid_NT (right, green) models. Corresponding bar plots show the R^2 values for five NT model setups in predicting monthly GPP (b), MSC (d), monthly anomaly (f), and cross-site variability (h).

3.1.2 Performance by biome and climate zone

The predictive ability of our models varied across different PFTs and Koppen climate zones (Figure 4). Here we present results from the CFE-Hybrid LT and ST models based on NT partitioning and note that patterns for the other CFE configurations and the DT GPP were similar (Figure S2).

Model performance in terms of monthly GPP was the highest for deciduous broadleaf forests, mixed forests, and evergreen needleleaf forests, with R^2 values above 0.78. Model accuracies were also high for savannas and grasslands, followed by croplands and wetlands, with R^2 values between 0.57 and 0.74. Model accuracies were lowest in evergreen broadleaf forests and shrublands, with R^2 values as low as 0.14. Across climate zones, models achieved the highest accuracy in predicting monthly GPP in cold and tropical climate zones with R^2 values between 0.64 and 0.80. The short-term models had the lowest performance in polar regions with an R^2 value of around 0.42, and the long-term model had the lowest performance in arid regions with an R^2 value of 0.25.

Model performance in terms of mean seasonal cycles across PFTs and climate zones followed patterns for monthly GPP, while disparities emerged for performance in terms of GPP anomaly and cross-site variability (Figure 4). The short-term model showed the highest predictive power in explaining monthly anomalies in arid regions with an R^2 value of 0.49, where savanna and shrublands sites are primarily located. Model performance in all other climate zones was significantly lower, with R^2 values below 0.2, and as low as 0.07 in temperate regions. Besides, the short-term model demonstrated good performance in capturing anomalies in deciduous broadleaf forests. The long-term model's relative performance between PFTs and climate zones was mostly consistent with that of the short-term model, with lower accuracy in shrublands when compared to the short-term model.

Models demonstrated the highest accuracy in predicting cross-site variability in savannas, grasslands, evergreen needleleaf forests, and evergreen broadleaf forests ($R^2 > 0.36$) and the lowest accuracy in deciduous broadleaf forests, mixed forests, and croplands ($R^2 < 0.20$). The short-term model additionally showed good performance in shrublands and wetlands ($R^2 > 0.36$), whereas the long-term model failed to capture any variability for shrublands. In terms of climate zones, models were most successful at explaining the variabilities within tropical and cold climate zones ($R^2 > 0.46$), the short-term model was least successful across polar regions, with a R^2 value of 0.29, and the long-term model had low performance for both polar and arid regions with R^2 values below 0.15.

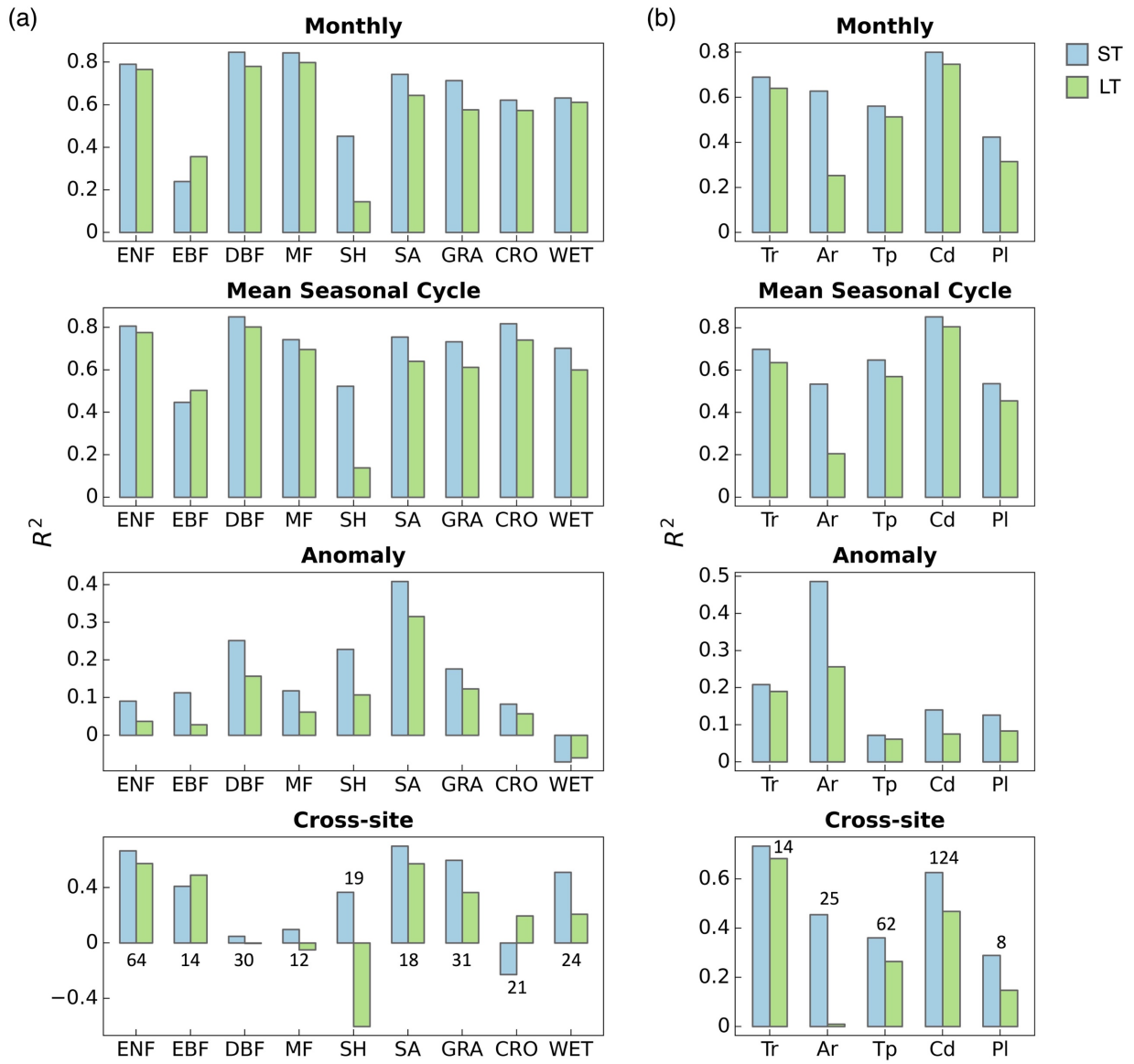

Figure 4. Performance of the ST_CFE-Hybrid_NT (blue) and LT_CFE-Hybrid_NT (green) models on GPP spatiotemporal estimation by plant functional types (a) and climate zones (b). The cross-site panels included the number of sites within each category. Color indicates short-term (ST) or long-term (LT) models. ENF: evergreen needleleaf forest, EBF: evergreen broadleaf forest, DBF: deciduous broadleaf forest, MF: mixed forest, SH: shrubland, SA: savanna, GRA: grassland, CRO: cropland, WET: wetland. Tr: tropical, Ar: arid, Tp: temperate, Cd: cold, Pl: polar. The performance of DT models is displayed in Supplementary Figure S2.

3.1.3 Prediction of long-term trends

Eddy covariance derived GPP presented a substantial increasing trend across flux sites between 2002 and 2019 (Figure 5a, Figure S3a). The eddy covariance GPP from the night-time

partitioning approach indicated an overall trend of 7.7 $gCm^{-2}year^{-2}$. In contrast, the ST_Baseline_NT model predicted a more modest trend of 2.7 $gCm^{-2}year^{-2}$, primarily reflecting the indirect CO_2 effect manifested through the growth of LAI. Both the ST_CFE-ML_NT and ST_CFE-hybrid_NT models predicted much higher trends of 5.5 and 4.3 $gCm^{-2}year^{-2}$ respectively, representing an improvement from the Baseline model by 51% and 29%, aligning more closely to eddy covariance observations. Similarly, the LT_CFE-Hybrid_NT model showed an improved trend estimation than the LT_Baseline_NT model. All trends were statistically significant ($p < 0.05$).

Aggregated eddy covariance GPP experienced increasing trends of varied magnitudes across different climate zones and plant functional types (Figure 5b,c; Figure S3b,c). While the machine learning models generally did not fully capture the enhancement in GPP for most categories, the CFE-ML and/or CFE-hybrid models consistently outperformed the Baseline models in both ST and LT setups. The CFE-ML setup predicted a higher trend than CFE-hybrid in most cases, suggesting that the data-driven approach captured more dynamics not represented in the theoretical model, which was based on conservative assumptions regarding the CO_2 sensitivity of photosynthesis (see Sect. 2.3.2 and Appendix A). The choice of remote sensing data (ST vs. LT configurations) did not lead to substantial differences in the predicted GPP trend. Most long-term flux sites (at least 10 years of records) with a significant trend experienced an increase in GPP, and the CFE-ML and/or CFE-hybrid models aligned closer to eddy covariance data than the Baseline models (Figure S4). Additionally, we found a considerably higher trend in eddy covariance GPP measurements derived from the day-time versus night-time partitioning approach, potentially associated with uncertainties in GPP partitioning methods (Figure S4). Yet, machine learning model predicted trends were not strongly affected by GPP partitioning methods (Figure S3, S4).

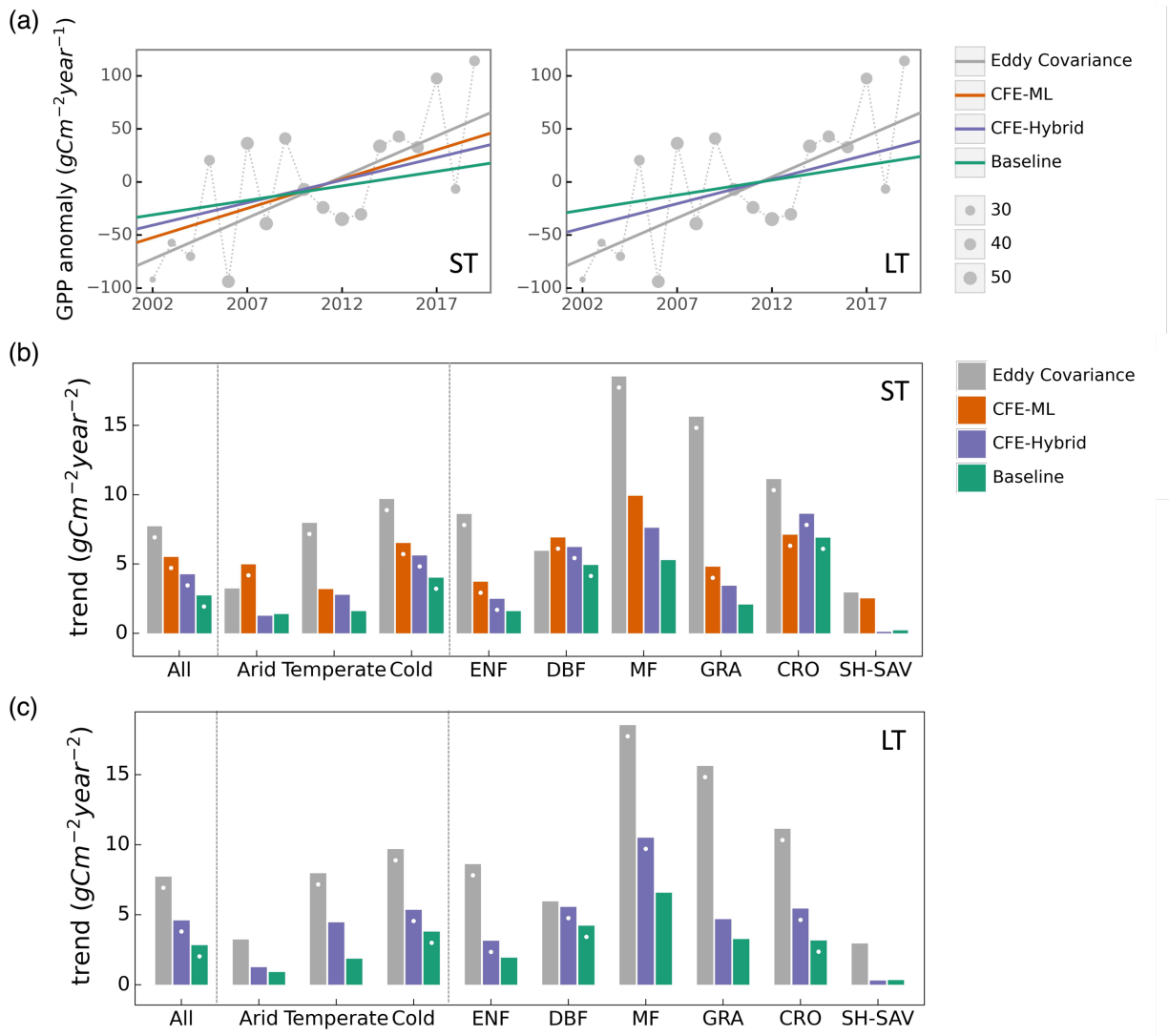

Figure 5. Comparison of observed and predicted GPP (from NT models only) trends across eddy covariance flux towers. (a) Aggregated annual GPP anomaly from 2002 to 2019 and trend lines from eddy covariance (EC) data, and three CFE model setups (short-term, night-time partitioning) for ST (left) and LT (right) models. The size of grey circle markers is proportional to the number of sites. (b) Comparison of annual GPP trends from eddy covariance measurements and the short-term (ST) CEDAR-GPP model setups by plant functional types and climate zones. (c) Comparison of annual GPP trends from eddy covariance measurements and the long-term (LT) CEDAR-GPP model setups by plant functional types and climate zones. In (b) and (c), Categories with less than 6 sites, including Tropics and EBF, were not shown. While dots on the bars indicate statistically significant trend with p-value < 0.1. Results for the DT models are shown in Supplementary Figure S3.

3.2 Evaluation of GPP spatial and temporal dynamics

We compared CEDAR-GPP estimates with other upscaled or LUE-based datasets regarding the mean annual GPP (Sect. 3.2.1), GPP seasonality (Sect. 3.2.2), interannual variability (Sect. 3.2.3), and annual trends (Sect. 3.2.4). CEDAR-GPP model setups generally showed similar patterns in mean annual GPP, seasonality, and interannual variability, therefore, in corresponding sections, we present the CFE-Hybrid model setups as representative examples for comparisons with other datasets, unless otherwise stated. Supplementary figures include comparisons involving CEDAR-GPP estimates from all model setups.

3.2.1 Mean annual GPP

Global patterns of mean annual GPP were generally consistent among CEDAR-GPP model setups, FLUXCOM, FLUXSAT, MODIS, and rEC-LUE, with few noticeable regional differences (Figure 6, Figure S5). Differences among CEDAR-GPP model setups were minimal and only evident between the NT and DT setups in the tropics (Figure 6b-c, Figure S5). CEDAR-GPP short-term datasets showed highest consistency with FLUXSAT in terms of mean annual GPP magnitudes (2001 – 2018) and latitudinal variations, although FLUXSAT presented slightly higher GPP values in the tropics compared to CEDAR-GPP (Figure 6b). Mean annual GPP magnitude for FLUXCOM-RS006 and MODIS was lower globally than CEDAR-GPP and FLUXSAT, with the most pronounced differences observed in the tropical areas. Among the long-term datasets (CEDAR-GPP LT, FLUXCOM-ERA5, and rEC-LUE), mean annual GPP (1982 – 2018) exhibited greater disparities in the northern mid-latitudes than in the tropics and southern hemisphere (Figure 6c). CEDAR-GPP aligned more closely with FLUXCOM-ERA5 than with rEC-LUE, with the latter showing lower annual mean GPP globally, particularly between 20ºN to 50º N.

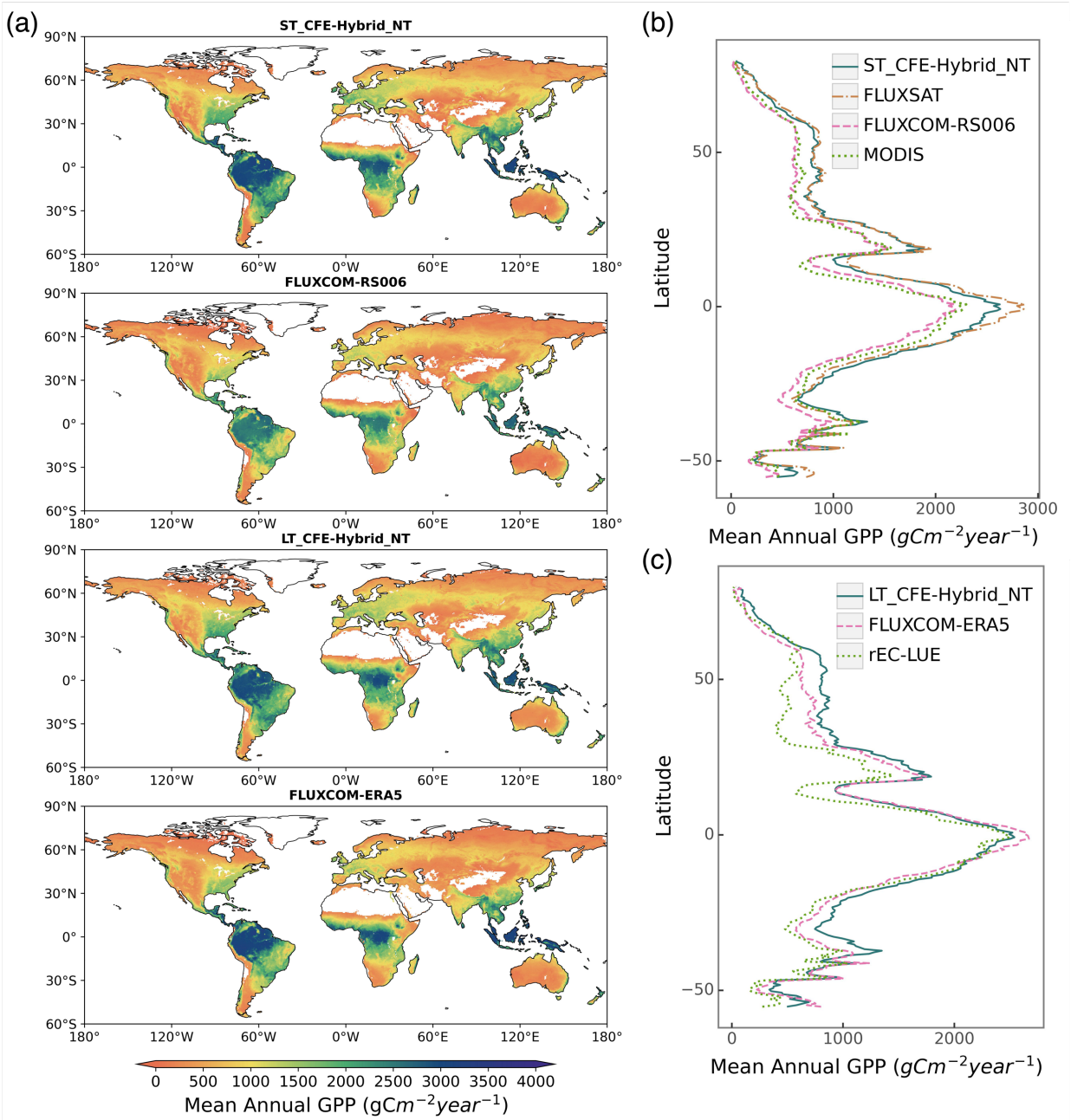

Figure 6. Global distributions of mean annual GPP from CEDAR-GPP and other machine learning upscaled and LUE-based reference datasets. (a) Global patterns of mean annual GPP from two short-term datasets including ST_CFE-Hybrid_NT, and FLUXCOM-RS006, and two long-term datasets including LT_CFE-Hybrid_NT, and FLUXCOM-ERA5. (b) Latitudinal distributions of mean annual GPP from short-term datasets (ST_CFE-Hybrid_NT, FLUXSAT, FLUXCOM-RS006, and MODIS). (c) Latitudinal distributions of mean annual GPP from long-term datasets (LT_CFE-Hybrid_NT, FLUXCOM-ERA5, and rEC-LUE). Mean annual GPP was computed between 2001 and 2018 for short-term datasets and between 1982 and 2018 for long-term datasets.

3.2.2 Seasonal variability

CEDAR-GPP and other machine learning upscaled or LUE-based GPP datasets agreed on seasonal variabilities (average between 2001 and 2018) at the global scale, characterized by a peak in GPP in July and a nadir between December and January (Figure 7, Figure S6, S7). At the global scale, CEDAR-GPP was most closely aligned with FLUXSAT in GPP seasonal magnitude and amplitude, while both FLUXCOM and MODIS displayed a relatively less pronounced magnitude.

In the northern hemisphere (20ºN - 90ºN), all GPP datasets agreed on seasonal GPP variation, despite variances in the magnitude of peak GPP. In the southern hemisphere (20ºS - 60ºS), all datasets exhibited their lowest GPP during June and July, and highest GPP from December to January. However, the seasonal amplitude of GPP was greatest for FLUXCOM-ERA5, followed by CEDAR-GPP and FLUXSAT, and substantially smaller for FLUXCOM-RS006 and MODIS GPP. In the tropics (20ºN - 20ºS), differences between datasets were the strongest, where seasonal variation is not as prominent compared to other regions. CEDAR-GPP, FLUXSAT, and FLUXCOM-ERA5 each showed two GPP peaks, occurring in March-April and September-October. Although FLUXCOM-RS006 had a similar seasonal pattern, its GPP magnitude was markedly smaller. Interestingly, MODIS showed an inverse season pattern with a small peak from June to August.

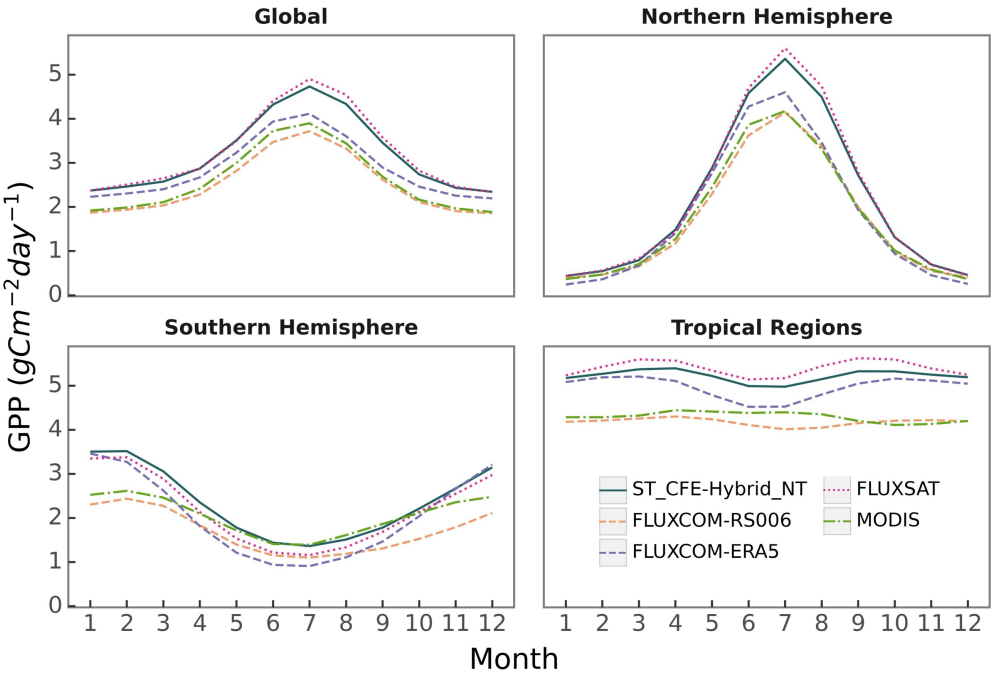

Figure 7. Comparison of GPP mean seasonal cycle between different datasets on a global scale, specifically within the Northern Hemisphere (20ºN - 90ºN), Southern

Hemisphere (20ºS - 60ºS), and Tropical regions (20ºN - 20ºS). Monthly means were averaged from 2001 to 2018 for all datasets.

3.2.3 Interannual variability

We found distinct spatial patterns in GPP interannual variability between upscaled and LUE-based datasets and a high level of agreement within each category, with the exception of FLUXCOM-ERA5, which showed minimal interannual variability globally (Figure 8, Figure S8). All datasets agreed on the presence of GPP interannual variability hotspots in eastern and southern South America, central North America, southern Africa, and western Australia. These hotspots primarily corresponded to arid and semi-arid areas characterized by grasslands, shrubs, and croplands (Figure 9). CEDAR-GPP was highly consistent with FLUXSAT, and both datasets also displayed relatively high interannual variability in the dry subhumid areas of Europe, predominately covered by croplands. FLUXCOM-RS006 mirrored the relative spatial patterns of CEDAR-GPP and FLUXSAT, albeit at lower magnitudes. The LUE-based datasets (MODIS and rEC-LUE) predicted a much higher interannual variability than the upscaled datasets in the tropical areas, particularly in evergreen broadleaf forests and woody savannas (Figure 8, Figure 9). These datasets also depicted slightly higher interannual variability for other types of forests, including evergreen needleleaf forests and deciduous broadleaf forests, compared to the upscaled datasets. The lack of interannual variability in FLUXCOM-ERA5 is attributable to the use of mean seasonal cycles of remotely sensed vegetation greenness indicators rather than their dynamic time series. Ten CEDAR-GPP model setups presented consistent patterns in interannual variability, and differences were minimal (Figure S8).

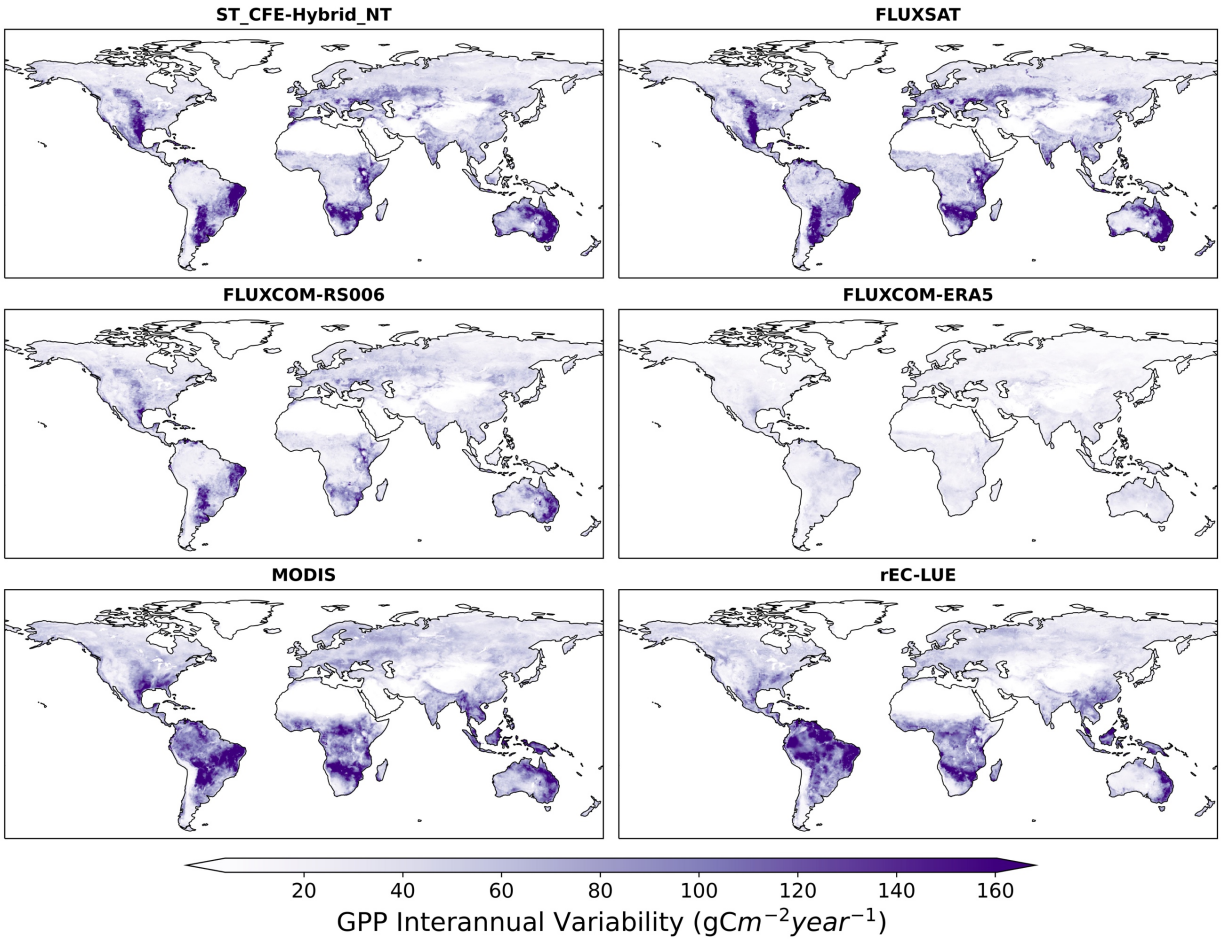

563

564 Figure 8. Spatial patterns of GPP interannual variability extracted over 2001 to 2018
565 for CEDAR-GPP (ST_CFE-Hybrid_NT), FLUXSAT, FLUXCOM-RS006, MODIS,
566 FLUXCOM-ERA5, and rEC-LUE.

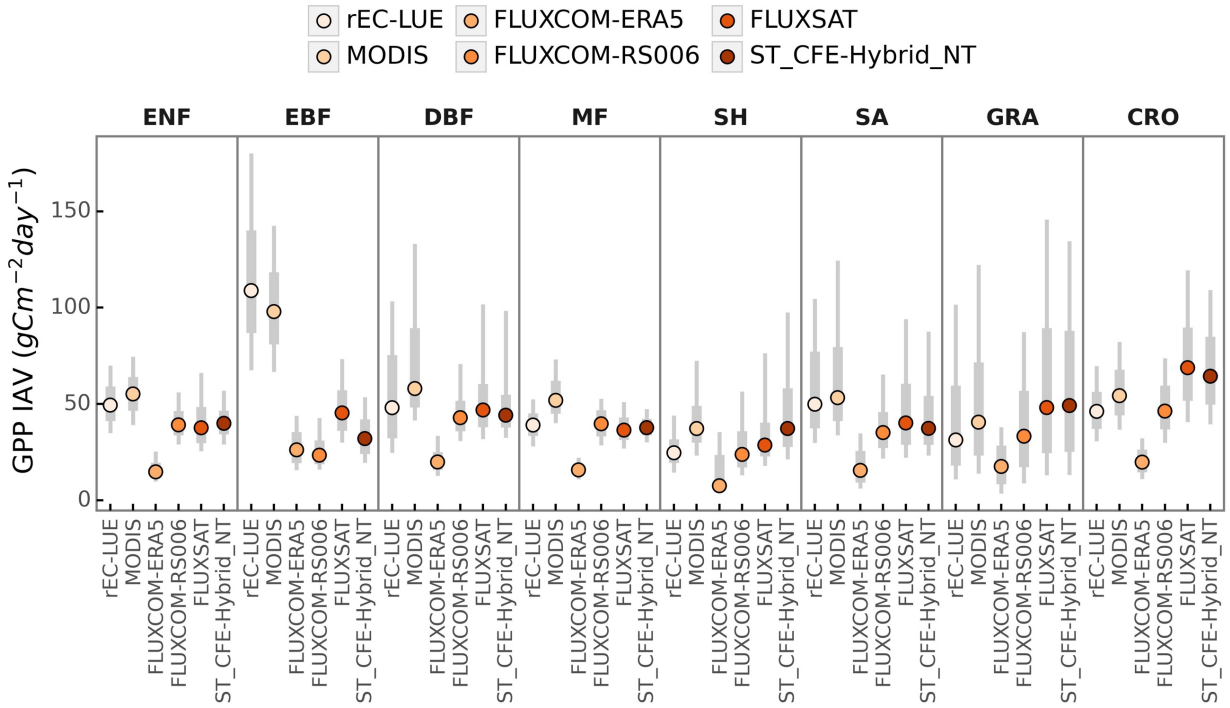

Figure 9. Comparison of GPP interannual variability (IAV) across global datasets by PFT. Colored dots represent the median IAV, thicker gray bars indicate the 25% to 75% percentiles of IAV distributions, and thinner grey bards show the 10% to 90% percentiles.

3.2.4 Trends

Differences in annual GPP trends among CEDAR-GPP model setups and other upscaled and LUE-based datasets mainly reflected the variability in the representation of CO_2 fertilization effects (Figure 10, Figure S9). From 2001 to 2018, the CEDAR-GPP Baseline model setups showed spatial variations in GPP trends consistent with the other upscaled datasets without direct CO_2 fertilization effects, including FLUXSAT and FLUXCOM-RSv006. In these datasets, substantial increases were seen in southeastern China and India, western Europe, and part of North and South America. These increases were largely associated with rising LAI due to land use changes and indirect CO_2 fertilization effects, as identified by previous studies (Chen et al., 2019; Zhu et al., 2016). Although MODIS, which also does not include a direct CO_2 fertilization effect, generally agreed with these increasing trends, it also showed a declining GPP in the tropical Amazon and a stronger positive trend in central South America. After incorporating the direct CO_2 fertilization effects, both the CFE-Hybrid and CFE-ML setups predicted positive trends in tropical forests, an observation absent in all other datasets. Furthermore, the CFE-Hybrid and CFE-ML models also revealed increasing

586 GPP in temperate and boreal forests of North America and Eurasia. Notably, all datasets agreed on
587 a pronounced GPP decrease in eastern Brazil.
588 From 2001 to 2018, a positive trend in global annual GPP was uniformly detected by all
589 datasets, albeit with varying magnitudes (Figure 11a-b). The ST_Baseline_NT model predicted a
590 GPP growth rate of 0.35 Pg C per year, aligning with FLUXCOM-RS, but lower than FLUXSAT
591 (0.51 Pg C yr^{-2}) and MODIS (0.39Pg C yr^{-2}) (Figure 11b). The CFE-hybrid models estimated a
592 notably faster GPP growth at 0.58 Pg C yr^{-2}. The CFE-ML models predicted the highest trends, up
593 to 0.76 Pg C yr^{-2} from the ST_CFE-ML_NT model and 0.59 Pg C yr^{-2} from the ST_CFE-ML_DT
594 model. Also, a higher variance was observed among ensemble members in the ST_CFE-ML setups
595 compared to the ST_Baseline and ST_CFE-Hybrid models.
596 The LT_Baseline_NT model identified increasing GPP trends in large areas of Europe, East
597 and South Asia, as well as the Northern Amazon from 1982 to 2020 (Figure 10b). The pattern from
598 the LT_CFE-Hybrid_NT model aligned closely with the LT_Baseline_NT model but exhibited a
599 stronger positive trend in global tropical areas as well as Eurasian boreal forests. In contrast,
600 FLUXCOM-ERA5 showed overall negative trends in the tropics, with a small magnitude. Lastly,
601 rEC-LUE agreed with positive GPP trends identified in CEDAR-GPP in the extratropical areas, but
602 predicted a pronounced negative trend in the tropics. At the global scale, all the CEDAR-GPP long-
603 term models predicted a positive global GPP trend (Figure 11d). The LT_Baseline models showed a
604 trend of 0.13 to 0.15 Pg C yr^{-2}, while the LT_CFE-Hybrid setups doubled that rate. rEC-LUE
605 showed a two-phased pattern with a strong increase in GPP from 1982 to 2000 (0.54 Pg C yr^{-2}),
606 followed by a decreasing trend after 2001 (-0.20 Pg C yr^{-2}) (Figure S10). This resulted in an overall
607 positive change at a rate comparable to that of the Baseline model. FLUXCOM-ERA5 exhibited a
608 small negative trend.

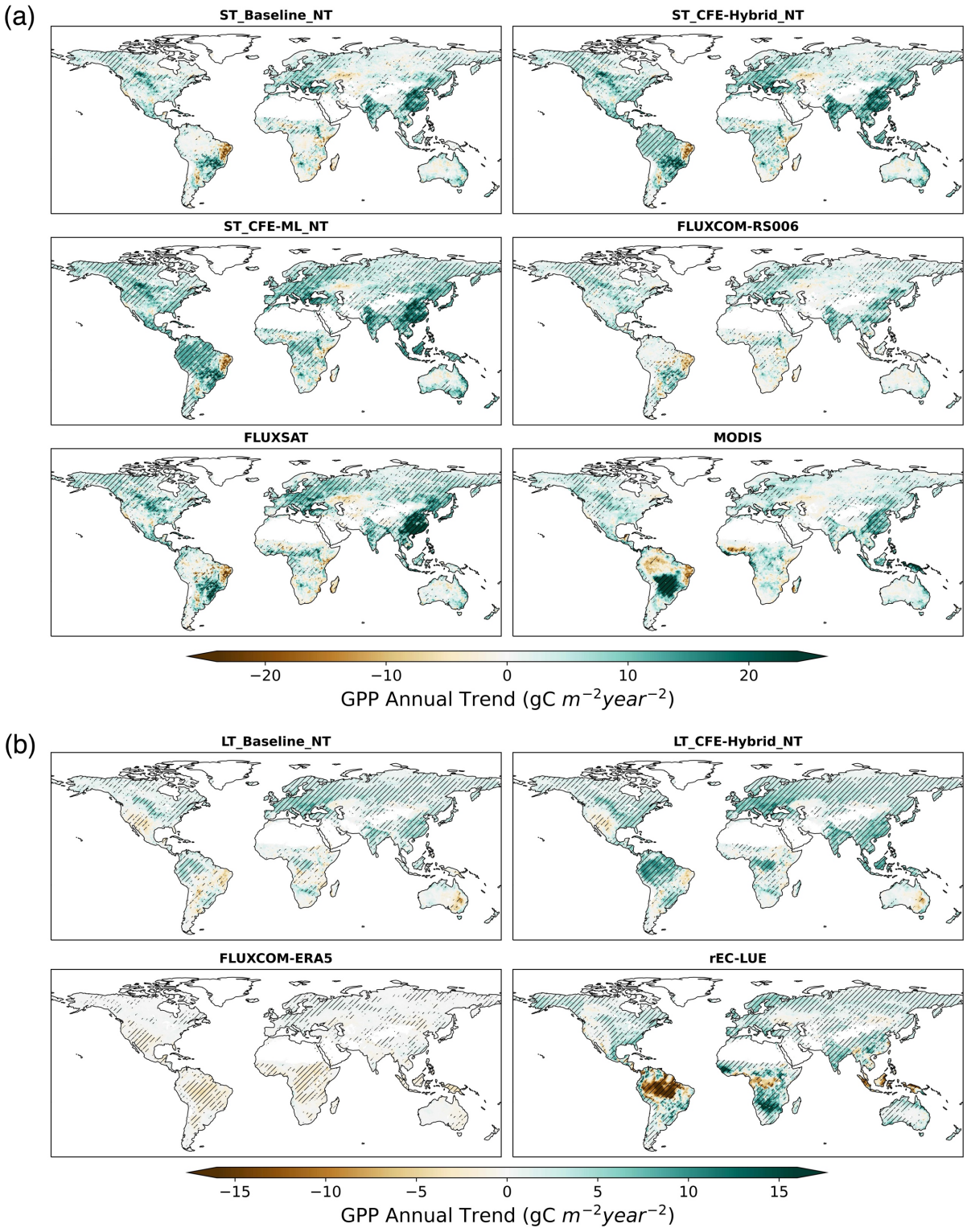

Figure 10. Annual GPP trend over 2001 – 2018 for short-term CEDAR-GPP, FLUXCOM-RS006, FLUXSAT, and MODIS datasets (a) and over 1982 – 2018 for long-term CEDAR-GPP, FLUXCOM-ERA5 and rEC-LUE datasets (b). Hatched

613 areas indicate the GPP trend that is statistically significant at $p < 0.05$ level under the
614 Mann-Kendal test.

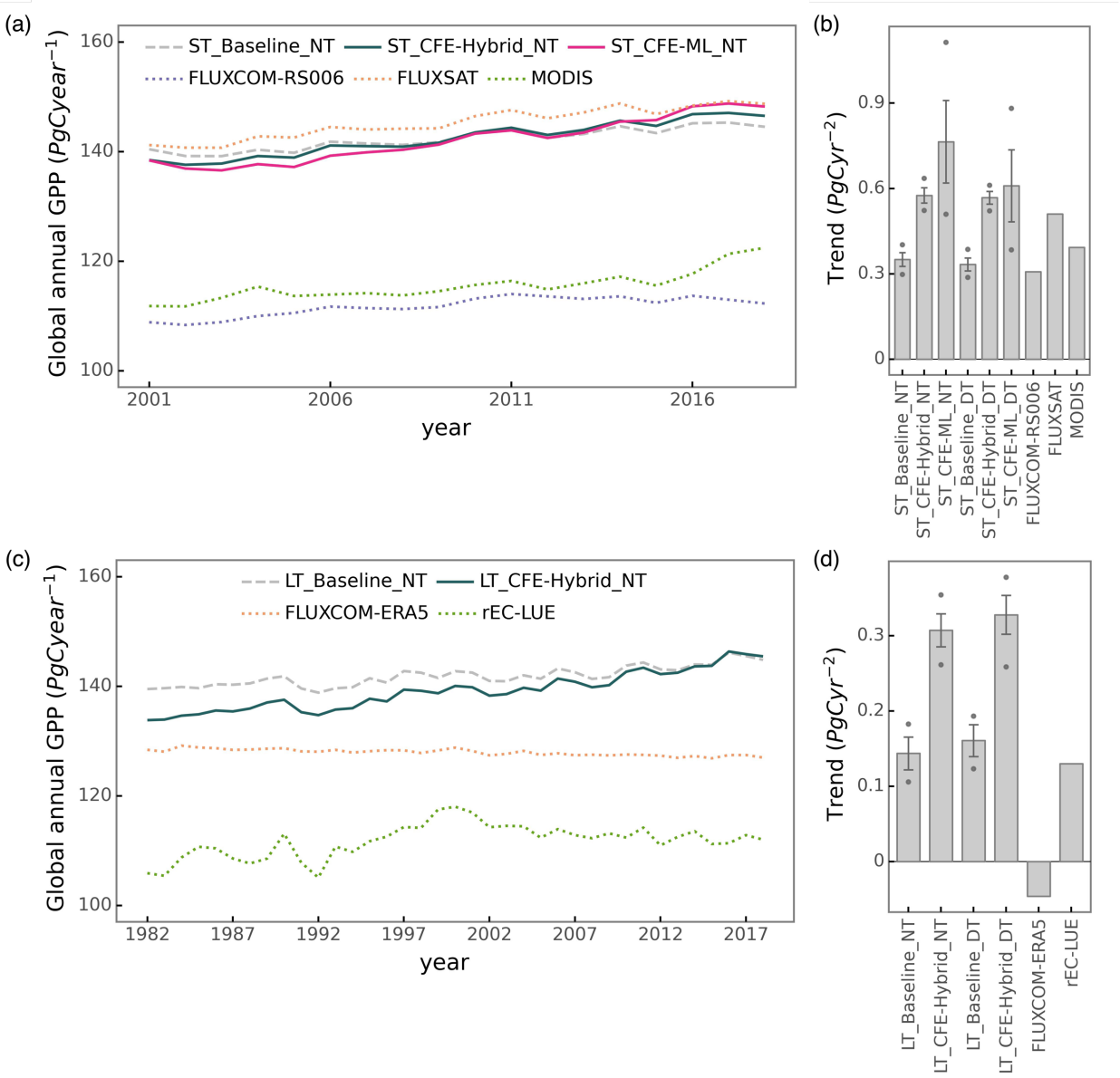

615

616 Figure 11. Global annual GPP variations (a) and trends (b) from 2001 to 2018 for
617 short-term CEDAR-GPP, FLUXCOM-RS006, FLUXSAT, and MODIS datasets.
618 Global annual GPP variations (c) and trends (d) over 1982 to 2018 for long-term for
619 long-term CEDAR-GPP, FLUXCOM-ERA5, and rEC-LUE datasets. Error bars in
620 (b) and (d) represent the 25% to 75% percentile from the model ensembles of
621 CEDAR-GPP. Dots in (b) and (d) indicate the minimum and maximum from the
622 model ensembles of CEDAR-GPP.

623

3.3 GPP estimation uncertainties

We analyzed the spread between the 30 model ensemble members in CEDAR-GPP as an indicator of uncertainties in GPP estimations. The spatial pattern of uncertainty in estimating annual mean GPP largely resembled that of the mean map (Figure 12, Figure 6a). The largest model spread was found in highly productive tropical forests, and this uncertainty decreased in temperate and cold areas (Figure 12a). Tropical ecosystems, with a mean annual GPP between 1000 to 3500 $PgCyr^{-1}$, only exhibited a 2% and 6% variation within the model ensemble (Figure 12b). Ecosystems in the temperate and cold climates had a smaller annual GPP and proportionally small uncertainties of up to 6%. However, ecosystems in Arid and Polar climates, despite their similarly low GPP, showed higher model uncertainty, reaching 10% to 40% of the ensemble mean. The estimation uncertainty of GPP trends was generally below 15% to 20% in the CEDAR-GPP datasets under the ST_Baseline and ST_CFE-Hybrid setups (Figure 12c). However, in the ST_CFE-ML setup, the estimation increased substantially, with model spread reaching up to 40% in tropical areas. Notably, the long-term models showed a higher uncertainty compared to the short-term models.

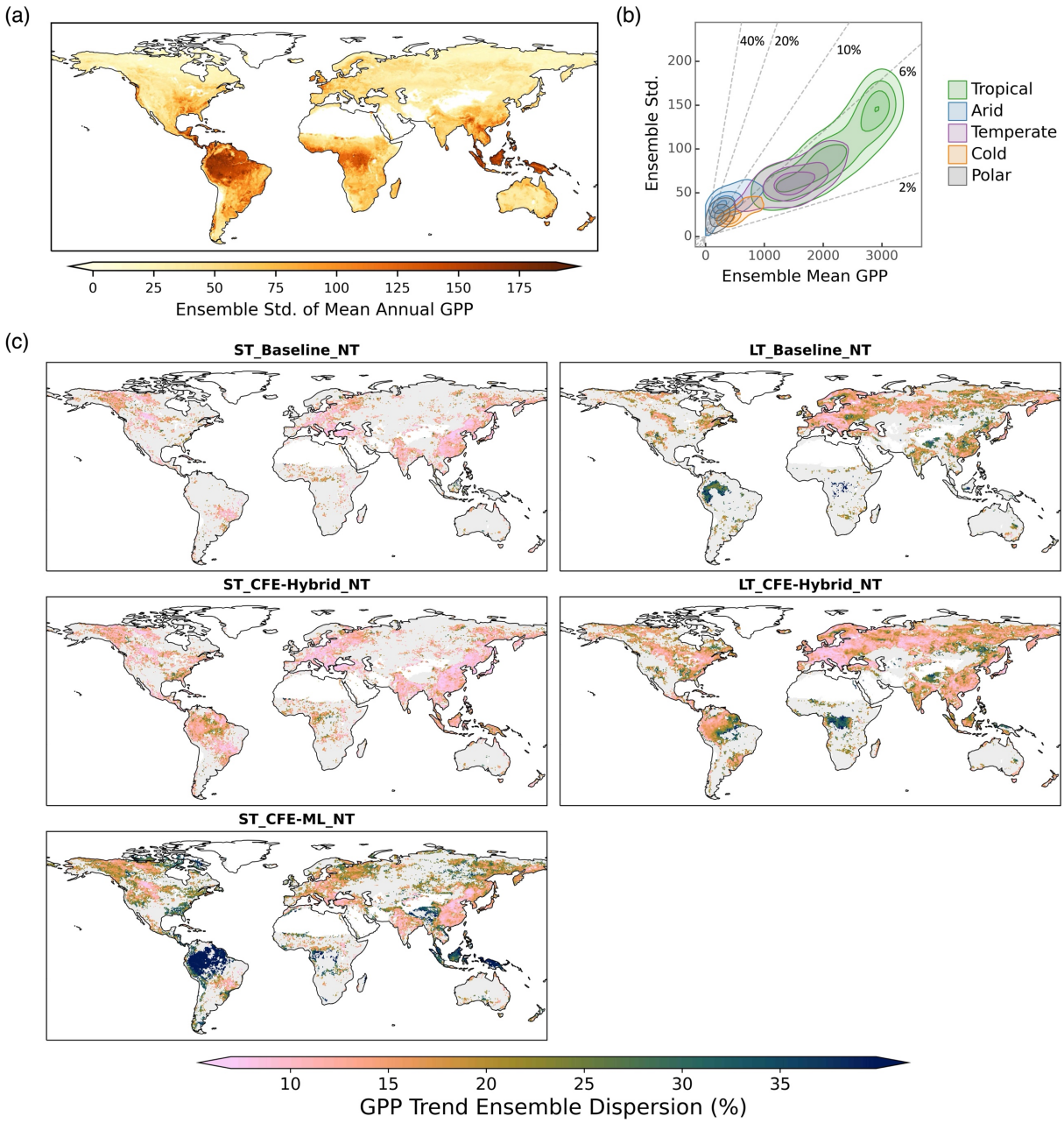

Figure 12. CEDAR-GPP estimation uncertainty derived from ensemble spread (standard deviation of 30 model predictions). (a) Spatial patterns of the absolute standard deviation from ensemble members in estimating the mean annual GPP from 2001 to 2018, using data from the ST_CFE-Hybrid_NT setup. (b) Relationships between ensemble standard deviation and ensemble mean in mean annual GPP. Colored contours denote clusters of Koppen climate zones. Dashed lines indicate the ratio between the ensemble standard deviation and the ensemble mean with values shown in percentage. (c) Spatial patterns of model uncertainty in GPP long-term trend estimation. Only areas where 90% of the ensemble members showed a statistically significant trend ($p<0.05$) are shown in the maps. The trend for the short-term datasets

(left column) was computed between 2001 to 2018. The trend for the long-term datasets (right column) was computed between 1982 to 2018.

4. Discussion

4.1 Reducing uncertainties in GPP upscaling

Here we examine the three predominate sources of uncertainties in machine learning upscaling of GPP: eddy covariance measurements, input datasets, and the machine learning model. We discuss strategies used in CEDAR-GPP to reduce the impacts of these uncertainties and highlight potential future research directions.

4.1.1 Eddy covariance data

Uncertainties associated with eddy covariance measurement and data processing can propagate through the upscaling process. CEDAR-GPP was produced using monthly aggregated eddy covariance data, where the impact of random errors in half-hourly measurements was minimized due to the temporal aggregation (Jung et al., 2020). Our stringent quality screening further reduced data processing uncertainties such as those associated with gap-filling. Yet, the discrepancy in GPP patterns between the CEDAR-GPP NT and DT setups is indicative of systematic biases linked to the partitioning approaches used to derive GPP from the Net Ecosystem Exchange measurements (Keenan et al., 2019; Pastorello et al., 2020). Interestingly, the mean annual GPP from the DT setup was slightly higher than that from the NT setup (Figure 6), and the DT setup also predicted a higher GPP trend in the long-term dataset (Figure 11). While these discrepancies were relatively small compared to the predominant spatiotemporal patterns, the separate DT and NT setups in CEDAR-GPP offered an interesting quantification of the GPP partitioning uncertainties over space and time, providing insights for future methodology improvements.

The unbalanced spatial representativeness of the eddy covariance data constitutes a more significant source of uncertainty, as highlighted by previous studies (Jung et al., 2020; Tramontana et al., 2015). Effective generalization of machine learning models requires a substantial volume of training data that adequately represents and balances varied conditions. In CEDAR-GPP, this issue was mitigated with a large set of eddy covariance data (~18000 site-months) integrating FLUXNET2015 and two regional networks. However, data availability remains limited in critical

carbon exchange hotspots such as tropical, subtropical, and boreal regions, as well as in mountainous areas (Figure 1). Contrary to widespread perception that sparse training data leads to high upscaling uncertainties, our findings from the bootstrapped model spread indicated modest uncertainties in tropical areas relative to their high GPP magnitude (Figure 12). This observation aligns with findings from the FLUXCOM product, revealing low extrapolation uncertainty in humid tropical regions (Jung et al., 2020). Additionally, an early study found that a machine learning model, when trained with simulated data from a terrestrial biosphere model that matches the locations and times of FLUXNET sites, could explain 92% of the global variation of GPP (Jung et al., 2009). These findings suggest that to fully understand the upscaling uncertainty, it is essential to evaluate the generalization or extrapolation errors within the predictor space, which indicates the environmental controls and physiological mechanisms of the ecosystem carbon fluxes (van der Horst et al., 2019; Villarreal and Vargas, 2021). Nevertheless, data limitations in mountainous areas and the absence of topology information in the predictor space in our models suggest potential uncertainties related to topographical effects on GPP (Hao et al., 2022; Xie et al., 2023).

Furthermore, our analysis suggested that the estimated global GPP magnitudes were related to the specific eddy covariance GPP data used in upscaling. Notably, global GPP magnitudes derived from CEDAR-GPP closely aligned with those from FLUXSAT, while the estimates from FLUXCOM were considerably lower (Figure 6, Figure 11). FLUXSAT used eddy covariance data from FLUXNET2015, which largely overlapped with that included in CEDAR-GPP (Joiner and Yoshida, 2020). FLUXCOM utilized data from FLUXNET La Thuile set and CarboAfrica network, which consisted of a distinct set of sites (Tramontana et al., 2016). The influence from the predictor datasets was minimal since all three datasets relied on MODIS-derived products. For a more in-depth evaluation of the impacts of flux site representativeness on upscaling, future research directions could include conducting synthetic experiments with simulations of ensembles of terrestrial biosphere models.

4.1.2 Input predictors and controlling factors

Upscaled GPP inherent uncertainties from the input predictors, including satellite and climate datasets. First, satellite remote sensing data contains noises resulting from sun-earth geometry, atmospheric conditions, soil background, and geolocation inaccuracies. The models or algorithms used for retrieving LAI, fAPAR, LST, and soil moisture, also contain random errors and systematic biases specific to certain regions, biome types, or climatic conditions (Fang et al., 2019; Ma et al.,

2019; Yan et al., 2016b). Moreover, satellite observations frequently contain missing values due to clouds, aerosols, snow, and algorithm failure, leading to both systematic and random uncertainties. In producing CEDAR-GPP, we mitigated these uncertainties through comprehensive preprocessing procedures. Our temporal gap-filling strategy exploited both the temporal dependency of vegetation status and long-term climatology, to reduce biases from missing values. Temporal and spatial aggregation further reduced the remaining data gaps and random noises. Nevertheless, considerable uncertainties likely remained in satellite datasets impacting the upscaled estimations.

A potentially more impactful source of uncertainty is the mismatch between the footprint of the eddy covariance measurements and the coarse resolution of satellite observations. While flux towers typically have a footprint of around ~1 km^2 (Chu et al., 2021), satellite observations employed in CEDAR-GPP and most other upscaled datasets were at 5 km or lower resolution. Systematic and random errors could be introduced due to this mismatch, particularly in heterogenous biomes and areas with a mixture of vegetation and non-vegetated land covers. One mitigation strategy is to generate upscaled datasets at a higher spatial resolution (e.g. 500m). Alternatively, models could be trained at a high resolution and applied to the coarse resolution to reduce computation and storage requirements (Dannenberg et al., 2023; Gaber et al., 2023). However, this approach does not address inherent scaling errors in coarse-resolution satellite images (Dong et al., 2023; Yan et al., 2016a).

Besides the quality of predictors, successful machine learning upscaling also requires a comprehensive set of features representing all controlling factors. For example, the lack of GPP interannual variabilities in FLUXCOM-ERA5 manifests the importance of incorporating dynamic vegetation signals from remote sensing in the upscaling framework. CEDAR-GPP used satellite observations from optical, thermal, and microwave systems as well as climate variables thoroughly representing GPP dynamics. Particularly, the inclusion of LST and soil moisture data provides important information about resource limitations and stress factors, which are crucial for certain biomes and/or under specific conditions (Green et al., 2022; Stocker et al., 2018, 2019). Dannenberg et al. (2023) showed that incorporating LST from MODIS and soil moisture from the SMAP satellite datasets substantially improved the machine learning estimation accuracy of GPP in North American drylands. Nevertheless, accurately capturing interannual anomalies remains challenging for certain biomes, such as evergreen needleleaf forest, cropland, and wetland (Figure 4), as acknowledged by previous studies (Tramontana et al., 2016; Jung et al., 2020). This suggests that vital information on GPP is missing or inadequately represented in existing datasets. To this end,

potential improvement may be achieved by incorporating datasets related to agricultural management practices (crop type, cultivar, irrigation, fertilization) (Xie et al., 2021), plant hydraulic and physiological properties (Liu et al., 2021), dynamic C4 plant distributions (Luo et al., 2024), root and soil characteristics (Stocker et al., 2023), as well as topography (Xie et al., 2023).

4.1.3 Machine learning models and uncertainty quantification

The choice of machine learning models and their parameterization has been found to have a relatively minor impact on GPP upscaling uncertainties (Tramontana et al., 2015). CEDAR used the state-of-the-art boosting algorithm, XGBoost, which provided high performance given the current data availability. Further reduction of model uncertainty will likely rely on additional information, such as increasing the number of eddy covariance sites or incorporating more high-quality predictors. Additionally, temporal dependency of carbon fluxes responses to atmospheric controls may also be exploited with specialized deep neural networks such as recurrent neural networks or transformers (Besnard et al., 2019; Ma and Liang, 2022).

A key challenge, however, is the quantification of uncertainties in machine learning upscaling (Reichstein et al., 2019). The limited availability of eddy covariance data hinders a comprehensive assessment of the extrapolation errors; consequently, metrics of predictive performance from cross-validation are inherently biased. CEDAR derived estimation uncertainty for each GPP prediction using bootstrapping model ensemble, which naturally mimics the sampling bias associated with flux tower locations. Notably, the choice of input climate reanalysis datasets could also induce systematic differences in GPP spatial and temporal patterns (Tramontana et al., 2015). As a result, the FLUXCOM product generates model ensembles based on different reanalysis datasets to capture these uncertainties. Additionally, different satellite datasets of vegetation structural proxies, such as LAI, also exhibited significant discrepancies (Jiang et al., 2017). Thus, an ensemble approach combining site-level bootstrapping with multiple sources of input predictors could potentially provide a more comprehensive quantification of uncertainties. Future work may also explore Bayesian neural networks, which provide uncertainty along with predictions and, at the same time, present high predictive power comparable to ensemble tree-based algorithms (Ma et al., 2021).

4.2 Long-term GPP changes and CO_2 fertilization effect

CEDAR-GPP was constructed using a comprehensive set of climate variables and multi-source satellite observations, thus, encapsulating long-term GPP dynamics from both direct and

771 indirect effects of climate controls. Particularly, CEDAR-GPP included the direct CO_2 fertilization
772 effect, which has been shown to dominate the increasing trend of global photosynthesis (Chen et al.,
773 2022). Incorporating these effects substantially improved long-term trends of GPP from site to
774 global scales (Figure 5, 10, 11). CEDAR's CFE-Hybrid setup offered a conservative estimation of
775 the direct CO_2 effects by simulating the CO_2 sensitivity of light-limited LUE for C3 plants (Walker
776 et al., 2021). However, the model did not account for the impacts of nutrient availability, which
777 could potentially constrain CO_2 fertilization (Peñuelas et al., 2017; Reich et al., 2014; Terrer et al.,
778 2019). Robust modeling of LUE responses to rising CO_2 under various environmental conditions
779 remains challenging (Wang et al., 2017). Future work is needed to better understand how these
780 factors affect the quantification of GPP and its long-term temporal variations.
781 The CFE-ML model adopted a data-driven approach to infer CO_2 effects directly from eddy
782 covariance data. This strategy allowed the model to capture any physiological pathways of the CO_2
783 impact evidenced in the eddy covariance measurements, including the increases of the biochemical
784 rates as well as enhancements in the water use efficiency (Keenan et al., 2013). The model
785 successfully detected a strong positive effect of CO_2 on eddy covariance measured GPP, consistent
786 with previous studies based on process-based and statistical models (Chen et al., 2022; Fernández-
787 Martínez et al., 2017; Ueyama et al., 2020). Notably, the CFE-ML model could have included the
788 impacts of other factors that exhibit a strong temporal correlation with CO_2. For example,
789 industrialization-induced increases in nitrogen deposition could synergistically boost GPP alongside
790 CO_2 (O'Sullivan et al., 2019). Technological and management improvements in agriculture that
791 contribute to a global enhancement of crop photosynthesis (Zeng et al., 2014), might also be
792 indirectly reflected in the model estimates. As a result, the CFE-ML predicted a GPP trend that
793 more closely aligned with eddy covariance observations, and the upscaled dataset also showed a
794 globally higher trend than CFE-Hybrid (Figure 5; Figure 10). Despite differences in magnitudes,
795 spatial patterns of GPP trends from the CFE-ML aligned with that from CFE-Hybrid, reflecting a
796 strong temperature dependency, implying that the effects of CO_2 likely remained the most
797 significant factor. Nonetheless, the considerable ensemble spread in the CO_2 trends from the CFE-
798 ML model and discrepancies between the CFE setups (Figure 11, Figure 13) underscored a high
799 level of uncertainty in the machine learning quantified CO_2 effects. Moreover, disentangling the
800 direct CO_2 effects on LUE, water use efficiency, and its indirect effects on LAI remains challenging
801 with machine learning models due to the correlations and interactions between CO_2 and other
802 climatic or environmental factors. Future work may exploit explainable machine learning and causal

inference to unravel the complex mechanisms and distinct pathways of CO_2 effects on vegetation carbon uptake.

Our results suggested that variations in the estimated GPP long-term trends from different products were largely related to the representation of CO_2 fertilization. Products that did not consider the direct CO_2 effect, including our Baseline models, FLUXSAT, FLUXCOM, and MODIS, showed minimal long-term changes in tropical GPP, while the CEDAR CFE-ML and CFE-Hybrid models demonstrated significant GPP increases aligning with predictions from the terrestrial biosphere models (Anav et al., 2015). FLUXCOM-ERA5, not accounting for dynamics changes in vegetation structures and CO_2, did not capture either the direct or indirect CO_2 fertilization resulting in a slight negative GPP trend attributable to shifted climate patterns. Notably, rEC-LUE exhibited contrasting trends before and after circa 2000, primarily attributed to changes in vapor pressure deficit, PAR, and LAI, while the direct CO_2 fertilization effect remained consistent (Zheng et al., 2020). Nevertheless, considerable differences between CEDAR-GPP and rEC-LUE, as well as between our CFE-ML and CFE-Hybrid products, warrant more in-depth investigations into long-term GPP responses to changes in atmospheric CO_2 and climate patterns.

Lastly, quantifications of GPP trends and their causes remain highly uncertain from site to global scales. Trend detection is often complicated by data noises and interannual variabilities, thus requiring long-term records which are limited in certain areas and biomes, such as tropics, polar regions, evergreen broadleaf forests and wetlands (Baldocchi et al., 2018; Zhan et al., 2022). Moreover, isolating the effect of CO_2 is challenging, as it is confounded by other factors, such as forest regrowth, land cover change, and disturbances, which also significantly impacts long-term GPP variations. To this end, continued efforts in expanding ecosystem flux measurements and standardizing data processing present new opportunities to assess ecosystem productivity responses to changing climate conditions (Delwiche et al., 2024; Pastorello et al., 2020). Future research could also leverage novel machine learning techniques, such as knowledge-guided machine learning (Liu et al., 2024) and hybrid modeling that combines process-based and machine learning approaches (Kraft et al., 2022; Reichstein et al., 2019).

5. Data availability and usage note

The CEDAR-GPP product, comprising ten GPP datasets, can be accessed at https://zenodo.org/doi/10.5281/zenodo.8212706 (Kang et al., 2024). These datasets were

generated at a spatial resolution of 0.05º and monthly time steps. Each dataset includes an ensemble mean GPP ("GPP_mean") and an ensemble standard deviation ("GPP_std"). Data is formatted in netCDF with the following naming convention: "CEDAR-GPP_<version>_<model setup>_<YYYYMM>.nc".

The CEDAR GPP product offers GPP estimates derived from ten different models. Models are characterized by 1) temporal coverage, 2) configuration of CO2 fertilization, and 3) GPP partitioning approach (Table 2). We provide a structured approach to selecting the most appropriate dataset for research or applications.

1) Study period considerations: the Short-Term (ST) setup is ideal for studies focusing on periods after 2000. These models are constructed using a broader range of explanatory predictors, offering higher precision and smaller random errors. The Long-Term (LT) datasets shall be used for research assessing GPP dynamics over a longer time period (before 2001). It is important to note that trends from the ST and LT datasets are not directly comparable, as they were derived from different satellite remote sensing data.

2) CO_2 Fertilization Effect (CFE) configurations: the CFE-Hybrid and CFE-ML setups are preferable when assessing temporal GPP dynamics, especially long-term trends. The CFE-Hybrid setup includes a hypothetical trend from the direct CO_2 effect, while CFE-ML is purely data-driven and does not make any specific assumption about the sensitivity of photosynthesis to CO_2. Averaging the CFE-Hybrid and CFE-ML estimates is acceptable, with the difference between them reflecting the uncertainty surrounding the direct CO_2 effect. Note that the Baseline setup shall not be used to study long-term GPP dynamics, especially those induced by elevated CO_2. Baseline setup may be useful to compare with other remote sensing-derived GPP datasets that do not consider the direct CO_2 effect. Differences between these setups regarding mean GPP spatial patterns, seasonal and interannual variations are considered to be minor.

3) GPP partitioning methods: We recommend using the mean value derived from both the "NT" (Nighttime) and "DT" (Daytime). The difference between these two provides insight into the uncertainties arising from the partitioning approaches used in GPP estimation from eddy covariance measurements.

6. Code availability

The code for upscaling and generating global GPP datasets can be accessed at https://doi.org/10.5281/zenodo.8400968.

7. Conclusions

We present the CEDAR-GPP product generated by upscaling global eddy covariance measurements with machine learning and a broad range of satellite and climate variables. CEDAR-GPP comprises four long-term datasets from 1982 to 2020 and six short-term datasets from 2001 to 2020. These datasets encompass three configurations regarding the incorporation of direct CO_2 fertilization effects and two partitioning approaches to derive GPP from eddy covariance data. The machine learning models of CEDAR-GPP demonstrated high capability in predicting monthly GPP, its seasonal cycles, and spatial variability within the global eddy covariance sites, with cross-validated R^2 between 0.56 to 0.79. Short-term model setups consistently outperformed long-term models due to considerably more and higher-quality information from multi-source satellite observations.

CEDAR-GPP advances satellite-based GPP estimations, as the first upscaled dataset that considered the direct biochemical effects of elevated atmospheric CO_2 on photosynthesis, which is responsible for an increasing land carbon sink over the past decades. We showed that incorporating this effect in our CFE-ML and CFE-Hybrid models substantially improved the estimation of GPP trends at eddy covariance sites. Global patterns of long-term GPP trends in the CFE-ML setups showed a strong temperature dependency consistent with biophysical theories. Aside from the trend, global spatial and temporal GPP patterns from CEDAR generally aligned with other satellite-based GPP datasets.

In conclusion, CEDAR-GPP, informed by global eddy covariance measurements and a broad range of multi-source remote sensing observations and climatic variables, offered a comprehensive representation of global GPP spatial and temporal dynamics over the past four decades. The different CO_2 fertilization configures integrated in CEDAR-GPP offer new opportunities for understanding global ecosystem photosynthesis's response to increases in atmospheric CO_2 along different pathways over space and time. CEDAR-GPP is expected to serve as a valuable tool for benchmarking process-based modeling and constraining the global carbon cycle.

Appendix A: CO_2 sensitivity function of Light Use Efficiency

In the CFE-Hybrid model, the direct CO_2 fertilization effect was prescribed onto machine learning estimated GPP at a reference CO_2 level using a theoretical CO_2 sensitivity function of LUE. The sensitivity function, which describes the fractional change in LUE due to CO_2 relative to the reference period, is described below.

The Light Use Efficiency (LUE) model (Monteith, 1972) of GPP states that,

$$GPP = APAR \times LUE = PAR \times fAPAR \times LUE \quad \text{(A1)}$$

where PAR is the photosynthetic active radiation, $fAPAR$ is the fraction of PAR that plant canopy has absorbed, and $APAR$ is the absorbed PAR. Eco-evolutionary theory, specifically the optimal coordination hypothesis, predicts that the electron-transport-limited (light-limited) (A_j) and Rubisco-limited (A_c) rates of photosynthesis converge on the time scale of physiological acclimation, which is in the order of a few weeks (Harrison et al., 2021; Haxeltine and Prentice, 1996; Wang et al., 2017). Thus, at a monthly time scale, we assume that

$$A = A_c = A_j \quad \text{(A2)}$$

where A is the gross photosynthetic rate, here equivalent to GPP.

In the following, we derive our sensitivity function based on A_j, which has a smaller response to CO_2 than A_c , thus providing conservative estimates of the direct CO_2 fertilization effect (Walker et al., 2021). According to the Fauquhar, von Caemmerer and Berry (FvCB) model (Farquhar et al., 1980),

$$A_j = \varphi_0 I \frac{c_i - \Gamma^*}{c_i + 2\Gamma^*} \quad \text{(A3)}$$

where φ_0 is the intrinsic quantum efficiency of photosynthesis, I is the absorbed PAR ($I = APAR$), c_i is the leaf-internal partial pressure of CO_2, and Γ^* is the photorespiratory compensation point that depends on temperature:

$$\Gamma^* = r_{25} e^{\frac{\Delta H(T - 298.15)}{298.15RT}} \quad \text{(A4)}$$

where $r_{25} = 4.22\ Pa$ is the photorespiratory point at 25 ºC, ΔH is the activation energy ($37.83 \cdot 10^3$ J mol^{-1}), T is the air temperature in Kelvin, and R is the molar gas constant (8.314 J mol^{-1} K^{-1}. We denote atmospheric CO_2 concentration as c_a, and χ is the ratio of leaf internal and external CO_2, so

$$c_i = \chi c_a \quad \text{(A5)}$$

Combing (A1), (A3), (A5), and assuming (A2), LUE can be written as,

$$LUE = \varphi_0 \frac{c_i - \Gamma^*}{c_i + 2\Gamma^*} = \varphi_0 \frac{\chi c_a - \Gamma^*}{\chi c_a + 2\Gamma^*} \quad \text{(A6)}$$

We can therefore show that under constant absorbed light (I or $APAR$), the sensitivity of GPP to CO_2 is proportional to that of LUE,

$$\frac{\partial GPP}{\partial c_a} = \frac{\partial \varphi_0 I \frac{\chi c_a - \Gamma^*}{\chi c_a + 2\Gamma^*}}{\partial c_a} = I \frac{\partial LUE}{\partial c_a} \quad \text{(A7)}$$

Thus from (A7), we can express the actual GPP at the time t and a CO_2 level c_a^t as the product of a reference GPP with a CO_2 level c_a^0 and the ratio between actual and reference LUE (A8-9). We denote the actual GPP as time t as $GPP^t_{c_a=c_a^t}$, and the reference GPP at time t as $GPP^t_{c_a=c_a^0}$.

$$\frac{GPP^t_{c_a=c_a^t}}{GPP^t_{c_a=c_a^0}} = \frac{LUE^t_{c_a=c_a^t}}{LUE^t_{c_a=c_a^0}} = \frac{\frac{\chi c_a^t - \Gamma^*}{\chi c_a^t + 2\Gamma^*}}{\frac{\chi c_a^0 - \Gamma^*}{\chi c_a^0 + 2\Gamma^*}} = \frac{\phi^t_{CO2}}{\phi^{t_0}_{CO2}} \quad \text{(A8)}$$

$$GPP^t_{c_a=c_a^t} = GPP^t_{c_a=c_a^0} \times \frac{\phi^t_{CO2}}{\phi^{t_0}_{CO2}} \quad \text{(A9)}$$

The reference GPP represents the GPP value at time t if the CO_2 were at the level of a reference level, while all other factors, such as PAR, $fAPAR$, temperature, and other environmental controls remain unchanged. Here the CO_2 impacts on LUE depend on atmospheric CO_2 (c_a), χ, and air temperature. We fixed χ to the global long-term average value 0.7 typical to C3 plants (Prentice et al., 2014; Wang et al., 2017). We further tested a dynamic model that quantified χ as a function of air temperature and vapor pressure deficit following an eco-evolutionary theory across global flux sites (Keenan et al., 2023). The estimated χ had a mean and median of 0.7 and a standard deviation of 0.04 (Figure S11a). Differences in the direct CO_2 effect between the dynamic and fixed χ approaches were minimal, with an R^2 of 0.99 and a slope of 0.99 from a least squares linear regression line (Figure S11b). GPP trends across flux towers were also highly consistent between the two approaches, with a difference less than 0.1 gC m^{-2} yr^{-2} (Figure S11b, c). Since these results indicated that χ is relatively stable, we used the fixed χ approach to produce the CEDAR-GPP dataset.

In the CFE-Hybrid model, we estimated the reference GPP by fixing the CO_2 at the level of the year 2001 while keeping all other variables dynamic in the CFE-ML model. Then the actual GPP can be estimated following (A9). Fixing CO_2 values to the 2001 level, the start year of eddy covariance data used in model training, essentially removed the effects of CO_2 inferred by the CFE-ML model.

Supplement

The supplement related to this article is available online.

Author contributions

T. K. and Y. K. conceptualized the study. Y. K. performed the formal analysis and generated the final product. Y. K., T. K., M. B., and M. G. contributed to the development and investigation of the research. Y. K., M. G., and X. L. contributed to data curation and processing. Y. K. prepared the manuscript with contributions from all co-authors. T. K. supervised the project.

Competing interests

The authors declare that they have no conflict of interest.

Acknowledgments

We are grateful to Dr. Youngryel Ryu for providing the BESS_Rad dataset and Dr. Martin Jung for sharing the FLUXCOM-RS006 dataset. We also thank Dr. Muyi Li, Dr. Zaichun Zhu, and Dr. Sen Cao for sharing early versions of the PKU GIMMS NDVI4g and LAI4g datasets with us.

Financial support

This research was supported by the U.S. Department of Energy Office of Science Early Career Research Program award #DE-SC0021023 and a NASA Award 80NSSC21K1705. TFK acknowledges additional support from the LEMONTREE (Land Ecosystem Models based On New Theory, obseRvations and ExperimEnts) project, funded through the generosity of Eric and Wendy Schmidt by recommendation of the Schmidt Futures programme and NASA award #80NSSC20K1801.

References

Anav, A., Friedlingstein, P., Beer, C., Ciais, P., Harper, A., Jones, C., Murray-Tortarolo, G., Papale, D., Parazoo, N. C., Peylin, P., Piao, S., Sitch, S., Viovy, N., Wiltshire, A., and Zhao, M.: Spatiotemporal patterns of terrestrial gross primary production: A review, Reviews of Geophysics, 1–34, https://doi.org/10.1002/2015RG000483, 2015.

Badgley, G., Anderegg, L. D. L., Berry, J. A., and Field, C. B.: Terrestrial gross primary production: Using NIRV to scale from site to globe, Global Change Biology, 25, 3731–3740, https://doi.org/10.1111/gcb.14729, 2019.

973 Baldocchi, D., Chu, H., and Reichstein, M.: Inter-annual variability of net and gross ecosystem
974 carbon fluxes: A review, Agricultural and Forest Meteorology, 249, 520–533,
975 https://doi.org/10.1016/j.agrformet.2017.05.015, 2018.

976 Baldocchi, D. D.: How eddy covariance flux measurements have contributed to our understanding
977 of Global Change Biology, Global Change Biology, 26, 242–260,
978 https://doi.org/10.1111/gcb.14807, 2020.

979 Beck, H. E., Zimmermann, N. E., McVicar, T. R., Vergopolan, N., Berg, A., and Wood, E. F.:
980 Present and future köppen-geiger climate classification maps at 1-km resolution, Scientific Data, 5,
981 1–12, https://doi.org/10.1038/sdata.2018.214, 2018.

982 Beer, C., Reichstein, M., Tomelleri, E., Ciais, P., Jung, M., Carvalhais, N., Rödenbeck, C., Arain, M.
983 A., Baldocchi, D., Bonan, G. B., Bondeau, A., Cescatti, A., Lasslop, G., Lindroth, A., Lomas, M.,
984 Luyssaert, S., Margolis, H., Oleson, K. W., Roupsard, O., Veenendaal, E., Viovy, N., Williams, C.,
985 Woodward, F. I., and Papale, D.: Terrestrial gross carbon dioxide uptake: Global distribution and
986 covariation with climate, Science, 329, 834–838, https://doi.org/10.1126/science.1184984, 2010.

987 Berdugo, M., Gaitán, J. J., Delgado-Baquerizo, M., Crowther, T. W., and Dakos, V.: Prevalence and
988 drivers of abrupt vegetation shifts in global drylands, Proceedings of the National Academy of
989 Sciences, 119, e2123393119, https://doi.org/10.1073/pnas.2123393119, 2022.

990 Besnard, S., Carvalhais, N., Altaf Arain, M., Black, A., Brede, B., Buchmann, N., Chen, J., Clevers, J.
991 G. P. W., Dutrieux, L. P., Gans, F., Herold, M., Jung, M., Kosugi, Y., Knohl, A., Law, B. E., Paul-
992 Limoges, E., Lohila, A., Merbold, L., Roupsard, O., Valentini, R., Wolf, S., Zhang, X., and
993 Reichstein, M.: Memory effects of climate and vegetation affecting net ecosystem CO2 fluxes in
994 global forests, PLoS ONE, 14, 1–22, https://doi.org/10.1371/journal.pone.0211510, 2019.

995 Bloomfield, K. J., Stocker, B. D., Keenan, T. F., and Prentice, I. C.: Environmental controls on the
996 light use efficiency of terrestrial gross primary production, Global Change Biology, 29, 1037–1053,
997 https://doi.org/10.1111/gcb.16511, 2023.

998 Campbell, J. E., Berry, J. A., Seibt, U., Smith, S. J., Montzka, S. A., Launois, T., Belviso, S., Bopp, L.,
999 and Laine, M.: Large historical growth in global terrestrial gross primary production, Nature, 544,
1000 84–87, https://doi.org/10.1038/nature22030, 2017.

1001 Camps-Valls, G., Campos-Taberner, M., Moreno-Martínez, Á., Walther, S., Duveiller, G., Cescatti,
1002 A., Mahecha, M. D., Muñoz-Marí, J., García-Haro, F. J., Guanter, L., Jung, M., Gamon, J. A.,
1003 Reichstein, M., and Running, S. W.: A unified vegetation index for quantifying the terrestrial
1004 biosphere, Science Advances, 7, eabc7447, https://doi.org/10.1126/sciadv.abc7447, 2021.

1005 Cao, S., Li, M., Zhu, Z., Zha, J., Zhao, W., Duanmu, Z., Chen, J., Zheng, Y., and Chen, Y.:
1006 Spatiotemporally consistent global dataset of the GIMMS Leaf Area Index (GIMMS LAI4g) from
1007 1982 to 2020, Earth System Science Data Discussions, 1–31, https://doi.org/10.5194/essd-2023-68,
1008 2023.

1009 Chen, C., Park, T., Wang, X., Piao, S., Xu, B., Chaturvedi, R. K., Fuchs, R., Brovkin, V., Ciais, P.,
1010 Fensholt, R., Tømmervik, H., Bala, G., Zhu, Z., Nemani, R. R., and Myneni, R. B.: China and India

lead in greening of the world through land-use management, Nature Sustainability, 2, 122–129, https://doi.org/10.1038/s41893-019-0220-7, 2019.

Chen, C., Riley, W. J., Prentice, I. C., and Keenan, T. F.: CO2 fertilization of terrestrial photosynthesis inferred from site to global scales, Proceedings of the National Academy of Sciences, 119, 1–8, https://doi.org/10.1073/pnas.2115627119/, 2022.

Chen, T. and Guestrin, C.: XGBoost: a scalable tree boosting system, in: Proceedings of the 22nd ACM SIGKDD International Conference on Knowledge Discovery and Data Mining - KDD '16, 785–794, https://doi.org/10.1145/2939672.2939785, 2016.

Chu, H., Luo, X., Ouyang, Z., Chan, W. S., Dengel, S., Biraud, S. C., Torn, M. S., Metzger, S., Kumar, J., Arain, M. A., Arkebauer, T. J., Baldocchi, D., Bernacchi, C., Billesbach, D., Black, T. A., Blanken, P. D., Bohrer, G., Bracho, R., Brown, S., Brunsell, N. A., Chen, J., Chen, X., Clark, K., Desai, A. R., Duman, T., Durden, D., Fares, S., Forbrich, I., Gamon, J. A., Gough, C. M., Griffis, T., Helbig, M., Hollinger, D., Humphreys, E., Ikawa, H., Iwata, H., Ju, Y., Knowles, J. F., Knox, S. H., Kobayashi, H., Kolb, T., Law, B., Lee, X., Litvak, M., Liu, H., Munger, J. W., Noormets, A., Novick, K., Oberbauer, S. F., Oechel, W., Oikawa, P., Papuga, S. A., Pendall, E., Prajapati, P., Prueger, J., Quinton, W. L., Richardson, A. D., Russell, E. S., Scott, R. L., Starr, G., Staebler, R., Stoy, P. C., Stuart-Haëntjens, E., Sonnentag, O., Sullivan, R. C., Suyker, A., Ueyama, M., Vargas, R., Wood, J. D., and Zona, D.: Representativeness of Eddy-Covariance flux footprints for areas surrounding AmeriFlux sites, Agricultural and Forest Meteorology, 301–302, https://doi.org/10.1016/j.agrformet.2021.108350, 2021.

Dannenberg, M. P., Barnes, M. L., Smith, W. K., Johnston, M. R., Meerdink, S. K., Wang, X., Scott, R. L., and Biederman, J. A.: Upscaling dryland carbon and water fluxes with artificial neural networks of optical, thermal, and microwave satellite remote sensing, Biogeosciences, 20, 383–404, https://doi.org/10.5194/bg-20-383-2023, 2023.

De Kauwe, M. G., Keenan, T. F., Medlyn, B. E., Prentice, I. C., and Terrer, C.: Satellite based estimates underestimate the effect of CO2 fertilization on net primary productivity, Nature Climate Change, 6, 892–893, https://doi.org/10.1038/nclimate3105, 2016.

Delwiche, K. B., Nelson, J., Kowalska, N., Moore, C. E., Shirkey, G., Tarin, T., Cleverly, J. R., and Keenan, T. F.: Charting the Future of the FLUXNET Network, Bulletin of the American Meteorological Society, 105, E466–E473, https://doi.org/10.1175/BAMS-D-23-0316.1, 2024.

Dong, Y., Li, J., Jiao, Z., Liu, Q., Zhao, J., Xu, B., Zhang, H., Zhang, Z., Liu, C., Knyazikhin, Y., and Myneni, R. B.: A Method for Retrieving Coarse-Resolution Leaf Area Index for Mixed Biomes Using a Mixed-Pixel Correction Factor, IEEE Transactions on Geoscience and Remote Sensing, 61, 1–17, https://doi.org/10.1109/TGRS.2023.3235949, 2023.

Dorigo, W., Wagner, W., Albergel, C., Albrecht, F., Balsamo, G., Brocca, L., Chung, D., Ertl, M., Forkel, M., Gruber, A., Haas, E., Hamer, P. D., Hirschi, M., Ikonen, J., de Jeu, R., Kidd, R., Lahoz, W., Liu, Y. Y., Miralles, D., Mistelbauer, T., Nicolai-Shaw, N., Parinussa, R., Pratola, C., Reimer, C., van der Schalie, R., Seneviratne, S. I., Smolander, T., and Lecomte, P.: ESA CCI Soil Moisture for improved Earth system understanding: State-of-the art and future directions, Remote Sensing of Environment, 203, 185–215, https://doi.org/10.1016/j.rse.2017.07.001, 2017.

Dorigo, W. A., Gruber, A., De Jeu, R. A. M., Wagner, W., Stacke, T., Loew, A., Albergel, C., Brocca, L., Chung, D., Parinussa, R. M., and Kidd, R.: Evaluation of the ESA CCI soil moisture product using ground-based observations, Remote Sensing of Environment, 162, https://doi.org/10.1016/j.rse.2014.07.023, 2015.

Ehlers, I., Augusti, A., Betson, T. R., Nilsson, M. B., Marshall, J. D., and Schleucher, J.: Detecting long-term metabolic shifts using isotopomers: CO2-driven suppression of photorespiration in C3 plants over the 20th century, Proceedings of the National Academy of Sciences, 112, 15585–15590, https://doi.org/10.1073/pnas.1504493112, 2015.

Fang, H., Baret, F., Plummer, S., and Schaepman-Strub, G.: An overview of global leaf area index (LAI): Methods, products, validation, and applications, Reviews of Geophysics, 2018RG000608, https://doi.org/10.1029/2018RG000608, 2019.

Farquhar, G. D., von Caemmerer, S., and Berry, J. A.: A biochemical model of photosynthetic CO2 assimilation in leaves of C3 species, Planta, 149, 78–90, https://doi.org/10.1007/BF00386231, 1980.

Fernández-Martínez, M., Vicca, S., Janssens, I. A., Ciais, P., Obersteiner, M., Bartrons, M., Sardans, J., Verger, A., Canadell, J. G., Chevallier, F., Wang, X., Bernhofer, C., Curtis, P. S., Gianelle, D., Grünwald, T., Heinesch, B., Ibrom, A., Knohl, A., Laurila, T., Law, B. E., Limousin, J. M., Longdoz, B., Loustau, D., Mammarella, I., Matteucci, G., Monson, R. K., Montagnani, L., Moors, E. J., Munger, J. W., Papale, D., Piao, S. L., and Peñuelas, J.: Atmospheric deposition, CO2, and change in the land carbon sink, Sci Rep, 7, 9632, https://doi.org/10.1038/s41598-017-08755-8, 2017.

Friedl, M. and Sulla-Menashe, D.: MCD12Q1 MODIS/Terra+Aqua Land Cover Type Yearly L3 Global 500m SIN Grid V006 [Data set], NASA EOSDIS Land Processes DAAC, https://doi.org/10.5067/MODIS/MCD12Q1.006, 2019.

Friedlingstein, P., Meinshausen, M., Arora, V. K., Jones, C. D., Anav, A., Liddicoat, S. K., and Knutti, R.: Uncertainties in CMIP5 climate projections due to carbon cycle feedbacks, Journal of Climate, 27, 511–526, https://doi.org/10.1175/JCLI-D-12-00579.1, 2014.

Friedlingstein, P., O'Sullivan, M., Jones, M. W., Andrew, R. M., Gregor, L., Hauck, J., Le Quéré, C., Luijkx, I. T., Olsen, A., Peters, G. P., Peters, W., Pongratz, J., Schwingshackl, C., Sitch, S., Canadell, J. G., Ciais, P., Jackson, R. B., Alin, S. R., Alkama, R., Arneth, A., Arora, V. K., Bates, N. R., Becker, M., Bellouin, N., Bittig, H. C., Bopp, L., Chevallier, F., Chini, L. P., Cronin, M., Evans, W., Falk, S., Feely, R. A., Gasser, T., Gehlen, M., Gkritzalis, T., Gloege, L., Grassi, G., Gruber, N., Gürses, Ö., Harris, I., Hefner, M., Houghton, R. A., Hurtt, G. C., Iida, Y., Ilyina, T., Jain, A. K., Jersild, A., Kadono, K., Kato, E., Kennedy, D., Klein Goldewijk, K., Knauer, J., Korsbakken, J. I., Landschützer, P., Lefèvre, N., Lindsay, K., Liu, J., Liu, Z., Marland, G., Mayot, N., McGrath, M. J., Metzl, N., Monacci, N. M., Munro, D. R., Nakaoka, S.-I., Niwa, Y., O'Brien, K., Ono, T., Palmer, P. I., Pan, N., Pierrot, D., Pocock, K., Poulter, B., Resplandy, L., Robertson, E., Rödenbeck, C., Rodriguez, C., Rosan, T. M., Schwinger, J., Séférian, R., Shutler, J. D., Skjelvan, I., Steinhoff, T., Sun, Q., Sutton, A. J., Sweeney, C., Takao, S., Tanhua, T., Tans, P. P., Tian, X., Tian, H., Tilbrook, B., Tsujino, H., Tubiello, F., van der Werf, G. R., Walker, A. P., Wanninkhof, R., Whitehead, C., Willstrand Wranne, A., et al.: Global Carbon Budget 2022, Earth System Science Data, 14, 4811–4900, 2023.

Gaber, M., Kang, Y., Schurgers, G., and Keenan, T.: Using automated machine learning for the upscaling of gross primary productivity, Biogeosciences Discussions, 1–26, https://doi.org/10.5194/bg-2023-141, 2023.

Gampe, D., Zscheischler, J., Reichstein, M., Sullivan, M. O., Smith, W. K., Sitch, S., and Buermann, W.: Increasing impact of warm droughts on northern ecosystem productivity over recent decades, Nature Climate Change, https://doi.org/10.1038/s41558-021-01112-8, 2021.

Gao, B. C.: NDWI - A normalized difference water index for remote sensing of vegetation liquid water from space, Remote Sensing of Environment, 58, 257–266, https://doi.org/10.1016/S0034-4257(96)00067-3, 1996.

Gitelson, A. A.: Remote estimation of leaf area index and green leaf biomass in maize canopies, Geophysical Research Letters, 30, 1248, https://doi.org/10.1029/2002GL016450, 2003.

Green, J. K., Ballantyne, A., Abramoff, R., Gentine, P., Makowski, D., and Ciais, P.: Surface temperatures reveal the patterns of vegetation water stress and their environmental drivers across the tropical Americas, Global Change Biology, 28, 2940–2955, https://doi.org/10.1111/gcb.16139, 2022.

Gruber, A., Scanlon, T., Van Der Schalie, R., Wagner, W., and Dorigo, W.: Evolution of the ESA CCI Soil Moisture climate data records and their underlying merging methodology, Earth System Science Data, 11, 717–739, https://doi.org/10.5194/essd-11-717-2019, 2019.

Hao, D., Bisht, G., Huang, M., Ma, P.-L., Tesfa, T., Lee, W.-L., Gu, Y., and Leung, L. R.: Impacts of Sub-Grid Topographic Representations on Surface Energy Balance and Boundary Conditions in the E3SM Land Model: A Case Study in Sierra Nevada, Journal of Advances in Modeling Earth Systems, 14, e2021MS002862, https://doi.org/10.1029/2021MS002862, 2022.

Harrison, S. P., Cramer, W., Franklin, O., Prentice, I. C., Wang, H., Brännström, Å., de Boer, H., Dieckmann, U., Joshi, J., Keenan, T. F., Lavergne, A., Manzoni, S., Mengoli, G., Morfopoulos, C., Peñuelas, J., Pietsch, S., Rebel, K. T., Ryu, Y., Smith, N. G., Stocker, B. D., and Wright, I. J.: Eco-evolutionary optimality as a means to improve vegetation and land-surface models, New Phytologist, https://doi.org/10.1111/nph.17558, 2021.

Haverd, V., Smith, B., Canadell, J. G., Cuntz, M., Mikaloff-Fletcher, S., Farquhar, G., Woodgate, W., Briggs, P. R., and Trudinger, C. M.: Higher than expected CO2 fertilization inferred from leaf to global observations, Global Change Biology, 26, 2390–2402, https://doi.org/10.1111/gcb.14950, 2020.

Haxeltine, A. and Prentice, I. C.: A General Model for the Light-Use Efficiency of Primary Production, Functional Ecology, 10, 551–561, https://doi.org/10.2307/2390165, 1996.

van der Horst, S. V. J., Pitman, A. J., De Kauwe, M. G., Ukkola, A., Abramowitz, G., and Isaac, P.: How representative are FLUXNET measurements of surface fluxes during temperature extremes?, Biogeosciences, 16, 1829–1844, https://doi.org/10.5194/bg-16-1829-2019, 2019.

Jiang, C., Ryu, Y., Fang, H., Myneni, R., Claverie, M., and Zhu, Z.: Inconsistencies of interannual variability and trends in long-term satellite leaf area index products, Global Change Biology, 23, 4133–4146, https://doi.org/10.1111/gcb.13787, 2017.

Joiner, J. and Yoshida, Y.: Satellite-based reflectances capture large fraction of variability in global gross primary production (GPP) at weekly time scales, Agricultural and Forest Meteorology, 291, 108092, https://doi.org/10.1016/j.agrformet.2020.108092, 2020.

Jung, M., Reichstein, M., and Bondeau, A.: Towards global empirical upscaling of FLUXNET eddy covariance observations: Validation of a model tree ensemble approach using a biosphere model, Biogeosciences, 6, 2001–2013, https://doi.org/10.5194/bg-6-2001-2009, 2009.

Jung, M., Reichstein, M., Margolis, H. A., Cescatti, A., Richardson, A. D., Arain, M. A., Arneth, A., Bernhofer, C., Bonal, D., Chen, J., Gianelle, D., Gobron, N., Kiely, G., Kutsch, W., Lasslop, G., Law, B. E., Lindroth, A., Merbold, L., Montagnani, L., Moors, E. J., Papale, D., Sottocornola, M., Vaccari, F., and Williams, C.: Global patterns of land-atmosphere fluxes of carbon dioxide , latent heat , and sensible heat derived from eddy covariance , satellite , and meteorological observations, Journal of Geophysical Research: Biogeosciences, 116, 1–16, https://doi.org/10.1029/2010JG001566, 2011.

Jung, M., Reichstein, M., Schwalm, C. R., Huntingford, C., Sitch, S., Ahlström, A., Arneth, A., Camps-Valls, G., Ciais, P., Friedlingstein, P., Gans, F., Ichii, K., Jain, A. K., Kato, E., Papale, D., Poulter, B., Raduly, B., Rödenbeck, C., Tramontana, G., Viovy, N., Wang, Y. P., Weber, U., Zaehle, S., and Zeng, N.: Compensatory water effects link yearly global land CO 2 sink changes to temperature, Nature, 541, 516–520, https://doi.org/10.1038/nature20780, 2017.

Jung, M., Schwalm, C., Migliavacca, M., Walther, S., Camps-Valls, G., Koirala, S., Anthoni, P., Besnard, S., Bodesheim, P., Carvalhais, N., Chevallier, F., Gans, F., S Goll, D., Haverd, V., Köhler, P., Ichii, K., K Jain, A., Liu, J., Lombardozzi, D., E M S Nabel, J., A Nelson, J., O'Sullivan, M., Pallandt, M., Papale, D., Peters, W., Pongratz, J., Rödenbeck, C., Sitch, S., Tramontana, G., Walker, A., Weber, U., and Reichstein, M.: Scaling carbon fluxes from eddy covariance sites to globe: Synthesis and evaluation of the FLUXCOM approach, Biogeosciences, 17, 1343–1365, https://doi.org/10.5194/bg-17-1343-2020, 2020.

Kang, Y., Ozdogan, M., Zhu, X., Ye, Z., Hain, C., and Anderson, M.: Comparative assessment of environmental variables and machine learning algorithms for maize yield prediction in the US Midwest, Environmental Research Letters, 15, https://doi.org/10.1088/1748-9326/ab7df9, 2020.

Kang, Y., Bassiouni, M., Gaber, M., Lu, X., and Keenan, T.: CEDAR-GPP: A Spatiotemporally Upscaled Dataset of Gross Primary Productivity Incorporating CO2 Fertilization (v1.0), https://doi.org/10.5281/zenodo.8212706, 2024.

Keeling, R. F., Graven, H. D., Welp, L. R., Resplandy, L., Bi, J., Piper, S. C., Sun, Y., Bollenbacher, A., and Meijer, H. A. J.: Atmospheric evidence for a global secular increase in carbon isotopic discrimination of land photosynthesis, Proceedings of the National Academy of Sciences of the United States of America, 114, 10361–10366, https://doi.org/10.1073/pnas.1619240114, 2017.

Keenan, T. F., Hollinger, D. Y., Bohrer, G., Dragoni, D., Munger, J. W., Schmid, H. P., and Richardson, A. D.: Increase in forest water-use efficiency as atmospheric carbon dioxide concentrations rise, Nature, 499, 324–327, https://doi.org/10.1038/nature12291, 2013.

Keenan, T. F., Prentice, I. C., Canadell, J. G., Williams, C. A., Wang, H., Raupach, M., and Collatz, G. J.: Recent pause in the growth rate of atmospheric CO2 due to enhanced terrestrial carbon uptake, Nature Communications, 7, 1–9, https://doi.org/10.1038/ncomms13428, 2016.

Keenan, T. F., Migliavacca, M., Papale, D., Baldocchi, D., Reichstein, M., Torn, M., and Wutzler, T.: Widespread inhibition of daytime ecosystem respiration, Nature Ecology and Evolution, 3, 407–415, https://doi.org/10.1038/s41559-019-0809-2, 2019.

Keenan, T. F., Luo, X., Stocker, B. D., De Kauwe, M. G., Medlyn, B. E., Prentice, I. C., Smith, N. G., Terrer, C., Wang, H., Zhang, Y., and Zhou, S.: A constraint on historic growth in global photosynthesis due to rising CO2, Nat. Clim. Chang., 1–6, https://doi.org/10.1038/s41558-023-01867-2, 2023.

Kraft, B., Jung, M., Körner, M., Koirala, S., and Reichstein, M.: Towards hybrid modeling of the global hydrological cycle, Hydrology and Earth System Sciences, 26, 1579–1614, https://doi.org/10.5194/hess-26-1579-2022, 2022.

Li, M., Cao, S., and Zhu, Z.: Spatiotemporally consistent global dataset of the GIMMS Normalized Difference Vegetation Index (PKU GIMMS NDVI) from 1982 to 2020, Earth System Science Data Discussions, 1–31, https://doi.org/10.5194/essd-2023-1, 2023.

Liu, L., Zhou, W., Guan, K., Peng, B., Xu, S., Tang, J., Zhu, Q., Till, J., Jia, X., Jiang, C., Wang, S., Qin, Z., Kong, H., Grant, R., Mezbahuddin, S., Kumar, V., and Jin, Z.: Knowledge-guided machine learning can improve carbon cycle quantification in agroecosystems, Nat Commun, 15, 357, https://doi.org/10.1038/s41467-023-43860-5, 2024.

Liu, Y., Holtzman, N. M., and Konings, A. G.: Global ecosystem-scale plant hydraulic traits retrieved using model–data fusion, Hydrology and Earth System Sciences, 25, 2399–2417, https://doi.org/10.5194/hess-25-2399-2021, 2021.

Luo, X., Zhou, H., Satriawan, T. W., Tian, J., Zhao, R., Keenan, T. F., Griffith, D. M., Sitch, S., Smith, N. G., and Still, C. J.: Mapping the global distribution of C4 vegetation using observations and optimality theory, Nat Commun, 15, 1219, https://doi.org/10.1038/s41467-024-45606-3, 2024.

Ma, H. and Liang, S.: Development of the GLASS 250-m leaf area index product (version 6) from MODIS data using the bidirectional LSTM deep learning model, Remote Sensing of Environment, 273, 112985, https://doi.org/10.1016/j.rse.2022.112985, 2022.

Ma, H., Zeng, J., Chen, N., Zhang, X., Cosh, M. H., and Wang, W.: Satellite surface soil moisture from SMAP, SMOS, AMSR2 and ESA CCI: A comprehensive assessment using global ground-based observations, Remote Sensing of Environment, 231, 111215, https://doi.org/10.1016/j.rse.2019.111215, 2019.

Ma, Y., Zhang, Z., Kang, Y., and Özdoğan, M.: Corn yield prediction and uncertainty analysis based on remotely sensed variables using a Bayesian neural network approach, Remote Sensing of Environment, 259, 112408, https://doi.org/10.1016/j.rse.2021.112408, 2021.

Myneni, R., Knyazikhin, Y., and Park, T.: MCD15A3H MODIS/Terra+Aqua Leaf Area Index/FPAR 4-day L4 Global 500m SIN Grid V006 [Data set], NASA EOSDIS Land Processes DAAC., https://doi.org/10.5067/MODIS/MCD15A3H.006, 2015a.

Myneni, R., Knyazikhin, Y., and Park, T.: MOD15A2H MODIS/Terra Leaf Area Index/FPAR 8-Day L4 Global 500m SIN Grid V006 [Data set], NASA EOSDIS Land Processes DAAC, https://doi.org/10.5067/MODIS/MOD15A2H.006, 2015b.

O'Sullivan, M., Spracklen, D. V., Batterman, S. A., Arnold, S. R., Gloor, M., and Buermann, W.: Have Synergies Between Nitrogen Deposition and Atmospheric CO 2 Driven the Recent Enhancement of the Terrestrial Carbon Sink?, Global Biogeochemical Cycles, 33, 163–180, https://doi.org/10.1029/2018GB005922, 2019.

O'Sullivan, M., Smith, W. K., Sitch, S., Friedlingstein, P., Arora, V. K., Haverd, V., Jain, A. K., Kato, E., Kautz, M., Lombardozzi, D., Nabel, J. E. M. S., Tian, H., Vuichard, N., Wiltshire, A., Zhu, D., and Buermann, W.: Climate-Driven Variability and Trends in Plant Productivity Over Recent Decades Based on Three Global Products, Global Biogeochemical Cycles, 34, https://doi.org/10.1029/2020GB006613, 2020.

Pastorello, G., Trotta, C., Canfora, E., Chu, H., Christianson, D., Cheah, Y. W., Poindexter, C., Chen, J., Elbashandy, A., Humphrey, M., Isaac, P., Polidori, D., Ribeca, A., van Ingen, C., Zhang, L., Amiro, B., Ammann, C., Arain, M. A., Ardö, J., Arkebauer, T., Arndt, S. K., Arriga, N., Aubinet, M., Aurela, M., Baldocchi, D., Barr, A., Beamesderfer, E., Marchesini, L. B., Bergeron, O., Beringer, J., Bernhofer, C., Berveiller, D., Billesbach, D., Black, T. A., Blanken, P. D., Bohrer, G., Boike, J., Bolstad, P. V., Bonal, D., Bonnefond, J. M., Bowling, D. R., Bracho, R., Brodeur, J., Brümmer, C., Buchmann, N., Burban, B., Burns, S. P., Buysse, P., Cale, P., Cavagna, M., Cellier, P., Chen, S., Chini, I., Christensen, T. R., Cleverly, J., Collalti, A., Consalvo, C., Cook, B. D., Cook, D., Coursolle, C., Cremonese, E., Curtis, P. S., D'Andrea, E., da Rocha, H., Dai, X., Davis, K. J., De Cinti, B., de Grandcourt, A., De Ligne, A., De Oliveira, R. C., Delpierre, N., Desai, A. R., Di Bella, C. M., di Tommasi, P., Dolman, H., Domingo, F., Dong, G., Dore, S., Duce, P., Dufrêne, E., Dunn, A., Dušek, J., Eamus, D., Eichelmann, U., ElKhidir, H. A. M., Eugster, W., Ewenz, C. M., Ewers, B., Famulari, D., Fares, S., Feigenwinter, I., Feitz, A., Fensholt, R., Filippa, G., Fischer, M., Frank, J., Galvagno, M., Gharun, M., Gianelle, D., et al.: The FLUXNET2015 dataset and the ONEFlux processing pipeline for eddy covariance data, Scientific data, 7, 225, https://doi.org/10.1038/s41597-020-0534-3, 2020.

Peñuelas, J., Ciais, P., Canadell, J. G., Janssens, I. A., Fernández-Martínez, M., Carnicer, J., Obersteiner, M., Piao, S., Vautard, R., and Sardans, J.: Shifting from a fertilization-dominated to a warming-dominated period, Nature Ecology and Evolution, 1, 1438–1445, https://doi.org/10.1038/s41559-017-0274-8, 2017.

Piao, S., Wang, X., Park, T., Chen, C., Lian, X., He, Y., Bjerke, J. W., Chen, A., Ciais, P., Tømmervik, H., Nemani, R. R., and Myneni, R. B.: Characteristics, drivers and feedbacks of global

greening, Nature Reviews Earth and Environment, 1, 14–27, https://doi.org/10.1038/s43017-019-0001-x, 2020.

Prentice, I. C., Dong, N., Gleason, S. M., Maire, V., and Wright, I. J.: Balancing the costs of carbon gain and water transport: testing a new theoretical framework for plant functional ecology, Ecology Letters, 17, 82–91, https://doi.org/10.1111/ele.12211, 2014.

Reich, P. B., Hobbie, S. E., and Lee, T. D.: Plant growth enhancement by elevated CO2 eliminated by joint water and nitrogen limitation, Nature Geoscience, 7, 920–924, https://doi.org/10.1038/ngeo2284, 2014.

Reichstein, M., Camps-Valls, G., Stevens, B., Jung, M., Denzler, J., Carvalhais, N., and Prabhat: Deep learning and process understanding for data-driven Earth system science, Nature, 566, 195–204, https://doi.org/10.1038/s41586-019-0912-1, 2019.

Ruehr, S., Keenan, T. F., Williams, C., Zhou, Y., Lu, X., Bastos, A., Canadell, J. G., Prentice, I. C., Sitch, S., and Terrer, C.: Evidence and attribution of the enhanced land carbon sink, Nat Rev Earth Environ, 1–17, https://doi.org/10.1038/s43017-023-00456-3, 2023.

Running, S., Mu, Q., and Zhao, M.: MOD17A2H MODIS/Terra Gross Primary Productivity 8-Day L4 Global 500m SIN Grid V006, https://doi.org/10.5067/MODIS/MOD17A2H.006, 2015.

Ryu, Y., Jiang, C., Kobayashi, H., and Detto, M.: MODIS-derived global land products of shortwave radiation and diffuse and total photosynthetically active radiation at 5 km resolution from 2000, Remote Sensing of Environment, 204, 812–825, https://doi.org/10.1016/j.rse.2017.09.021, 2018.

Ryu, Y., Berry, J. A., and Baldocchi, D. D.: What is global photosynthesis? History, uncertainties and opportunities, Remote Sensing of Environment, 223, 95–114, https://doi.org/10.1016/j.rse.2019.01.016, 2019.

Sabater, J. M.: ERA5-Land monthly averaged data from 1981 to present., Copernicus Climate Change Service (C3S) Climate Data Store (CDS), https://doi.org/doi:10.24381/cds.68d2bb30, 2019.

Schaaf, C. and Wang, Z.: MCD43C4 MODIS/Terra+Aqua BRDF/Albedo Nadir BRDF-Adjusted Ref Daily L3 Global 0.05Deg CMG V006 [Data set], NASA EOSDIS Land Processes DAAC., https://doi.org/10.5067/MODIS/MCD43C4.006, 2015.

Schwalm, C. R., Anderegg, W. R. L., Michalak, A. M., Fisher, J. B., Biondi, F., Koch, G., Litvak, M., Ogle, K., Shaw, J. D., Wolf, A., Huntzinger, D. N., Schaefer, K., Cook, R., Wei, Y., Fang, Y., Hayes, D., Huang, M., Jain, A., and Tian, H.: Global patterns of drought recovery, Nature, 548, 202–205, https://doi.org/10.1038/nature23021, 2017.

Smith, W. K., Reed, S. C., Cleveland, C. C., Ballantyne, A. P., Anderegg, W. R. L., Wieder, W. R., Liu, Y. Y., and Running, S. W.: Large divergence of satellite and Earth system model estimates of global terrestrial CO2 fertilization, Nature Climate Change, 6, 306–310, https://doi.org/10.1038/nclimate2879, 2016.

Ștefan, V. and Levin, S.: plotbiomes: R package for plotting Whittaker biomes with ggplot2, , https://doi.org/10.5281/zenodo.7145245, 2018.

Still, C. J., Berry, J. A., Collatz, G. J., and DeFries, R. S.: Global distribution of C3 and C4 vegetation: Carbon cycle implications, Global Biogeochemical Cycles, 17, https://doi.org/10.1029/2001gb001807, 2003.

Still, C. J., Berry, J. A., Collatz, G. J., and DeFries, R. S.: ISLSCP II C4 Vegetation Percentage, in: Hall, Forrest G., G. Collatz, B. Meeson, S. Los, E. Brown de Colstoun, and D. Landis (eds.). ISLSCP Initiative II Collection. Data set., http://dx.doi.org/10.3334/ORNLDAAC/932, 2009.

Stocker, B. D., Zscheischler, J., Keenan, T. F., Prentice, I. C., Peñuelas, J., and Seneviratne, S. I.: Quantifying soil moisture impacts on light use efficiency across biomes, New Phytologist, 218, 1430–1449, https://doi.org/10.1111/nph.15123, 2018.

Stocker, B. D., Zscheischler, J., Keenan, T. F., Prentice, I. C., Seneviratne, S. I., and Peñuelas, J.: Drought impacts on terrestrial primary production underestimated by satellite monitoring, Nature Geoscience, 12, 264–270, https://doi.org/10.1038/s41561-019-0318-6, 2019.

Stocker, B. D., Tumber-Dávila, S. J., Konings, A. G., Anderson, M. C., Hain, C., and Jackson, R. B.: Global patterns of water storage in the rooting zones of vegetation, Nat. Geosci., 16, 250–256, https://doi.org/10.1038/s41561-023-01125-2, 2023.

Terrer, C., Jackson, R. B., Prentice, I. C., Keenan, T. F., Kaiser, C., Vicca, S., Fisher, J. B., Reich, P. B., Stocker, B. D., Hungate, B. A., Peñuelas, J., McCallum, I., Soudzilovskaia, N. A., Cernusak, L. A., Talhelm, A. F., Van Sundert, K., Piao, S., Newton, P. C. D., Hovenden, M. J., Blumenthal, D. M., Liu, Y. Y., Müller, C., Winter, K., Field, C. B., Viechtbauer, W., Van Lissa, C. J., Hoosbeek, M. R., Watanabe, M., Koike, T., Leshyk, V. O., Polley, H. W., and Franklin, O.: Nitrogen and phosphorus constrain the CO2 fertilization of global plant biomass, Nature Climate Change, 9, 684–689, https://doi.org/10.1038/s41558-019-0545-2, 2019.

Thoning, K. W., Crotwell, A. M., and Mund, J. W.: Atmospheric Carbon Dioxide Dry Air Mole Fractions from continuous measurements at Mauna Loa, Hawaii, Barrow, Alaska, American Samoa and South Pole. 1973-2020, Version 2021-08-09, National Oceanic and Atmospheric Administration (NOAA), Global Monitoring Laboratory (GML), Boulder, Colorado, USA, https://doi.org/10.15138/yaf1-bk21, 2021.

Tramontana, G., Ichii, K., Camps-Valls, G., Tomelleri, E., and Papale, D.: Uncertainty analysis of gross primary production upscaling using Random Forests, remote sensing and eddy covariance data, Remote Sensing of Environment, 168, 360–373, https://doi.org/10.1016/j.rse.2015.07.015, 2015.

Tramontana, G., Jung, M., Schwalm, C. R., Ichii, K., Camps-Valls, G., Ráduly, B., Reichstein, M., Arain, M. A., Cescatti, A., Kiely, G., Merbold, L., Serrano-Ortiz, P., Sickert, S., Wolf, S., and Papale, D.: Predicting carbon dioxide and energy fluxes across global FLUXNET sites with regression algorithms, Biogeosciences, 13, 4291–4313, https://doi.org/10.5194/bg-13-4291-2016, 2016.

Ueyama, M., Ichii, K., Kobayashi, H., Kumagai, T., Beringer, J., Merbold, L., Euskirchen, E. S., Hirano, T., Marchesini, L. B., Baldocchi, D., Saitoh, T. M., Mizoguchi, Y., Ono, K., Kim, J., Varlagin, A., Kang, M., Shimizu, T., Kosugi, Y., Bret-Harte, M. S., Machimura, T., Matsuura, Y., Ohta, T., Takagi, K., Takanashi, S., and Yasuda, Y.: Inferring CO2 fertilization effect based on

global monitoring land-atmosphere exchange with a theoretical model, Environmental Research Letters, 15, 84009, https://doi.org/10.1088/1748-9326/ab79e5, 2020.

Villarreal, S. and Vargas, R.: Representativeness of FLUXNET Sites Across Latin America, Journal of Geophysical Research: Biogeosciences, 126, e2020JG006090, https://doi.org/10.1029/2020JG006090, 2021.

Walker, A. P., De Kauwe, M. G., Bastos, A., Belmecheri, S., Georgiou, K., Keeling, R. F., McMahon, S. M., Medlyn, B. E., Moore, D. J. P., Norby, R. J., Zaehle, S., Anderson-Teixeira, K. J., Battipaglia, G., Brienen, R. J. W., Cabugao, K. G., Cailleret, M., Campbell, E., Canadell, J. G., Ciais, P., Craig, M. E., Ellsworth, D. S., Farquhar, G. D., Fatichi, S., Fisher, J. B., Frank, D. C., Graven, H., Gu, L., Haverd, V., Heilman, K., Heimann, M., Hungate, B. A., Iversen, C. M., Joos, F., Jiang, M., Keenan, T. F., Knauer, J., Körner, C., Leshyk, V. O., Leuzinger, S., Liu, Y., MacBean, N., Malhi, Y., McVicar, T. R., Penuelas, J., Pongratz, J., Powell, A. S., Riutta, T., Sabot, M. E. B., Schleucher, J., Sitch, S., Smith, W. K., Sulman, B., Taylor, B., Terrer, C., Torn, M. S., Treseder, K. K., Trugman, A. T., Trumbore, S. E., van Mantgem, P. J., Voelker, S. L., Whelan, M. E., and Zuidema, P. A.: Integrating the evidence for a terrestrial carbon sink caused by increasing atmospheric CO2, New Phytologist, 229, 2413–2445, https://doi.org/10.1111/nph.16866, 2021.

Walther, S., Besnard, S., Nelson, J. A., El-Madany, T. S., Migliavacca, M., Weber, U., Carvalhais, N., Ermida, S. L., Brümmer, C., Schrader, F., Prokushkin, A. S., Panov, A. V., and Jung, M.: Technical note: A view from space on global flux towers by MODIS and Landsat: the FluxnetEO data set, Biogeosciences, 19, 2805–2840, https://doi.org/10.5194/bg-19-2805-2022, 2022.

Wan, Z., Hook, S., and Hulley, G.: MOD11A1 MODIS/Terra Land Surface Temperature/Emissivity Daily L3 Global 1km SIN Grid V006 [Data set], NASA EOSDIS Land Processes DAAC, https://doi.org/10.5067/MODIS/MOD11A1.006, 2015a.

Wan, Z., Hook, S., and Hulley, G.: MYD11A1 MODIS/Aqua Land Surface Temperature/Emissivity Daily L3 Global 1km SIN Grid V006 [Data set], NASA EOSDIS Land Processes DAAC, https://doi.org/10.5067/MODIS/MYD11A1.006, 2015b.

Wang, H., Prentice, I. C., Keenan, T. F., Davis, T. W., Wright, I. J., Cornwell, W. K., Evans, B. J., and Peng, C.: Towards a universal model for carbon dioxide uptake by plants, Nature Plants, 3, 734–741, https://doi.org/10.1038/s41477-017-0006-8, 2017.

Warm Winter 2020 Team: Warm Winter 2020 ecosystem eddy covariance flux product for 73 stations in FLUXNET-Archive format—release 2022-1 (Version 1.0), https://doi.org/10.18160/2G60-ZHAK, 2022.

Wenzel, S., Cox, P. M., Eyring, V., and Friedlingstein, P.: Projected land photosynthesis constrained by changes in the seasonal cycle of atmospheric CO2, Nature, 538, 499–501, https://doi.org/10.1038/nature19772, 2016.

Xiao, J., Zhuang, Q., Baldocchi, D. D., Law, B. E., Richardson, A. D., Chen, J., Oren, R., Starr, G., Noormets, A., Ma, S., Verma, S. B., Wharton, S., Wofsy, S. C., Bolstad, P. V., Burns, S. P., Cook, D. R., Curtis, P. S., Drake, B. G., Falk, M., Fischer, M. L., Foster, D. R., Gu, L., Hadley, J. L., Hollinger, D. Y., Katul, G. G., Litvak, M., Martin, T. A., Matamala, R., McNulty, S., Meyers, T. P., Monson, R. K., Munger, J. W., Oechel, W. C., Paw U, K. T., Schmid, H. P., Scott, R. L., Sun, G., Suyker, A. E.,

and Torn, M. S.: Estimation of net ecosystem carbon exchange for the conterminous United States by combining MODIS and AmeriFlux data, Agricultural and Forest Meteorology, 148, 1827–1847, https://doi.org/10.1016/j.agrformet.2008.06.015, 2008.

Xie, X., Chen, J. M., Yuan, W., Guan, X., Jin, H., and Leng, J.: A Practical Algorithm for Correcting Topographical Effects on Global GPP Products, Journal of Geophysical Research: Biogeosciences, 128, e2023JG007553, https://doi.org/10.1029/2023JG007553, 2023.

Xie, Y., Gibbs, H. K., and Lark, T. J.: Landsat-based Irrigation Dataset (LANID): 30m resolution maps of irrigation distribution, frequency, and change for the US, 1997–2017, Earth System Science Data, 13, 5689–5710, https://doi.org/10.5194/essd-13-5689-2021, 2021.

Yan, K., Park, T., Yan, G., Chen, C., Yang, B., Liu, Z., Nemani, R. R., Knyazikhin, Y., and Myneni, R. B.: Evaluation of MODIS LAI/FPAR product collection 6. Part 1: Consistency and improvements, Remote Sensing, 8, 1–16, https://doi.org/10.3390/rs8050359, 2016a.

Yan, K., Park, T., Yan, G., Liu, Z., Yang, B., Chen, C., Nemani, R. R., Knyazikhin, Y., and Myneni, R. B.: Evaluation of MODIS LAI/FPAR product collection 6. Part 2: Validation and intercomparison, Remote Sensing, 8, 460, https://doi.org/10.3390/rs8060460, 2016b.

Yang, F., Ichii, K., White, M. A., Hashimoto, H., Michaelis, A. R., Votava, P., Zhu, A. X., Huete, A., Running, S. W., and Nemani, R. R.: Developing a continental-scale measure of gross primary production by combining MODIS and AmeriFlux data through Support Vector Machine approach, Remote Sensing of Environment, 110, 109–122, https://doi.org/10.1016/j.rse.2007.02.016, 2007.

Yang, R., Wang, J., Zeng, N., Sitch, S., Tang, W., McGrath, M. J., Cai, Q., Liu, D., Lombardozzi, D., Tian, H., Jain, A. K., and Han, P.: Divergent historical GPP trends among state-of-the-art multi-model simulations and satellite-based products, Earth System Dynamics, 13, 833–849, https://doi.org/10.5194/esd-13-833-2022, 2022.

Yuan, H., Dai, Y., Xiao, Z., Ji, D., and Shangguan, W.: Reprocessing the MODIS Leaf Area Index products for land surface and climate modelling, Remote Sensing of Environment, 115, 1171–1187, https://doi.org/10.1016/j.rse.2011.01.001, 2011.

Zeng, J., Matsunaga, T., Tan, Z.-H., Saigusa, N., Shirai, T., Tang, Y., Peng, S., and Fukuda, Y.: Global terrestrial carbon fluxes of 1999–2019 estimated by upscaling eddy covariance data with a random forest, Sci Data, 7, 313, https://doi.org/10.1038/s41597-020-00653-5, 2020.

Zeng, N., Zhao, F., Collatz, G. J., Kalnay, E., Salawitch, R. J., West, T. O., and Guanter, L.: Agricultural Green Revolution as a driver of increasing atmospheric CO2 seasonal amplitude, Nature, 515, 394–397, https://doi.org/10.1038/nature13893, 2014.

Zhan, C., Orth, R., Migliavacca, M., Zaehle, S., Reichstein, M., Engel, J., Rammig, A., and Winkler, A. J.: Emergence of the physiological effects of elevated CO2 on land–atmosphere exchange of carbon and water, Global Change Biology, 28, 7313–7326, https://doi.org/10.1111/gcb.16397, 2022.

Zhang, Y.: A global spatially contiguous solar-induced fluorescence (CSIF) dataset using neural networks (2000-2020), National Tibetan Plateau Data Center, https://doi.org/10.11888/Ecolo.tpdc.271751., 2021.

Zhang, Y., Joiner, J., Hamed Alemohammad, S., Zhou, S., and Gentine, P.: A global spatially contiguous solar-induced fluorescence (CSIF) dataset using neural networks, Biogeosciences, 15, 5779–5800, https://doi.org/10.5194/bg-15-5779-2018, 2018.

Zheng, Y., Shen, R., Wang, Y., Li, X., Liu, S., Liang, S., Chen, J. M., Ju, W., Zhang, L., and Yuan, W.: Improved estimate of global gross primary production for reproducing its long-Term variation, 1982-2017, Earth System Science Data, 12, 2725–2746, https://doi.org/10.5194/essd-12-2725-2020, 2020.

Zhu, Z., Piao, S., Myneni, R. B., Huang, M., Zeng, Z., Canadell, J. G., Ciais, P., Sitch, S., Friedlingstein, P., Arneth, A., Cao, C., Cheng, L., Kato, E., Koven, C., Li, Y., Lian, X., Liu, Y., Liu, R., Mao, J., Pan, Y., Peng, S., Peuelas, J., Poulter, B., Pugh, T. A. M., Stocker, B. D., Viovy, N., Wang, X., Wang, Y., Xiao, Z., Yang, H., Zaehle, S., and Zeng, N.: Greening of the Earth and its drivers, Nature Climate Change, 6, 791–795, https://doi.org/10.1038/nclimate3004, 2016.